

# Selective glycerol to lactic acid conversion *via* a tandem effect between platinum and metal oxides with abundant acid groups

Hui Luo,<sup>1,2</sup>† Mianle Xu,<sup>3</sup>† Sihang Liu,<sup>3</sup> Giulia Tarantino,<sup>1</sup> Hossein Yadegari,<sup>4</sup> Alain Y. Li,<sup>1</sup> Karen Chan,<sup>3</sup> Ceri Hammond,<sup>1</sup> Georg Kastlunger,<sup>3\*</sup> Ifan E. L. Stephens,<sup>4\*</sup> Maria-Magdalena Titirici<sup>1\*</sup>

1. Department of Chemical Engineering, Imperial College London, South Kensington Campus, SW7 2AZ, London, UK
2. School of Mechanical Engineering Sciences, University of Surrey, Stag Hill Campus, GU2 7XH, Guildford, UK
3. Catalysis Theory Center, Department of Physics, Technical University of Denmark (DTU), 2800 Kgs. Lyngby, Denmark
4. Department of Materials, Imperial College London, South Kensington Campus, SW7 2AZ, London, UK

† These authors contributed equally.

Corresponding Author:

\* [geokast@dtu.dk](mailto:geokast@dtu.dk) (Georg Kastlunger)

\* [i.stephens@imperial.ac.uk](mailto:i.stephens@imperial.ac.uk) (Ifan E. L. Stephens)

\* [m.titirici@imperial.ac.uk](mailto:m.titirici@imperial.ac.uk) (Maria-Magdalena Titirici)

## Abstract

Phasing out petrochemical-based thermoplastics with bio-plastics produced in an energy efficient and environmentally friendly way is of paramount interest. Among them, polylactic acid (PLA) is the flagship with its production accounting for 19% of the entire bioplastics industry. Glycerol electrolysis for producing the monomer lactic acid, while co-generating green H<sub>2</sub>, represents a promising approach to boost the production of PLA, yet the reaction selectivity has been a bottleneck. Here, we report a combined electrochemical and chemical route using a tandem Pt/C- $\gamma$ -Al<sub>2</sub>O<sub>3</sub> multicomponent catalyst which can achieve a glycerol-to-lactic acid selectivity of 60.2 ± 2.7%, among the highest performance reported so far. Combining an experimental and computational mechanistic analysis, we suggest that tuning the acidic sites on catalyst surface is crucial for shifting the reaction towards the dehydration pathway, occurring *via* dihydroxyacetone intermediate. Within the tandem effect, Pt is the active site to electrochemically catalyze glycerol to dihydroxyacetone and glyceraldehyde, while the  $\gamma$ -Al<sub>2</sub>O<sub>3</sub> provides the required acidic sites for catalyzing dihydroxyacetone to the pyruvaldehyde

intermediate, which will then go through Cannizzaro rearrangement, catalyzed by the OH<sup>-</sup> ions to form lactic acid. This catalytic synergy improves the selectivity towards lactic acid by nearly two-fold. A selectivity descriptor ( $\Delta G_{GLAD}^* - \Delta G_{DHA}^*$ ) from density functional theory calculations was identified, which could be used to screen other materials in further research. Our findings highlight the promise of tandem electrolysis in the development of strategies for selective electrochemical production of high-value commodity chemicals from low value (waste) precursors.

## Introduction

The chemical sector consumes vast amounts of oil and gas, accounting for 15% of total primary demand for oil on a volumetric basis and 9% of gas. The use of fossil-fuels as feedstock and energy source, also dictates its unsustainability with direct CO<sub>2</sub> emission of 880 Mt in 2018.<sup>1</sup> Among all the products in the chemical sector, petrochemical based thermoplastics have an annual production of 222 Mt yr<sup>-1</sup> in total.<sup>2</sup> Globally, these plastics are becoming less attractive to consumers, brands and governments. This shift has made bio-based and bio-degradable plastics a viable, responsible and intelligent alternative to facilitate the transformation towards a zero-emission chemical industry.<sup>3</sup>

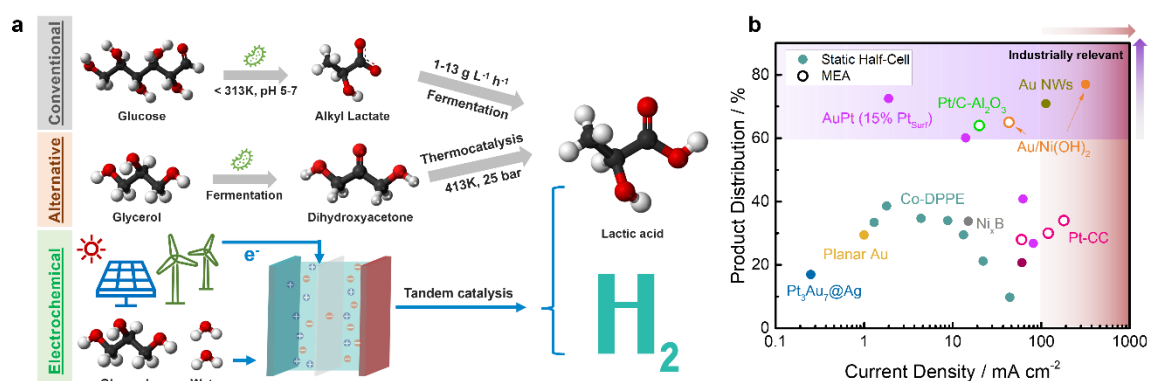


**Fig.1** | **a.** Illustrations of three different technique routes to produce lactic acid; **b.** Benchmark of literature reported values of electrochemical glycerol conversion to lactic acid. The liquid product distribution towards lactic acid is defined as: mole of lactic acid/mole of total liquid products detected  $\times$  100%. Other detectable liquid products include: glyceric acid, tartronic acid, glycolic acid, oxalic acid. (Source of references: Co-DPPE<sup>4</sup>; Pt<sub>3</sub>Au<sub>7</sub>@Ag<sup>5</sup>; Pt-CBAC<sup>6</sup>; Pt-CC<sup>7</sup>; Ni<sub>x</sub>Bi<sub>1-x</sub><sup>8</sup>; Planar Au<sup>9</sup>; Au NWs<sup>10,11</sup>; Au/Ni(OH)<sub>2</sub><sup>10,11</sup>; AuPt (15% Pt<sub>Surf</sub>)<sup>12</sup>) To note the use of liquid product distribution towards lactic acid is for literature comparison. In the discussion below, more standard quantification methods with product yield and faradaic efficiency are used throughout this work.

Poly(lactic acid) (PLA) is a bio-based polyester and the most utilized degradable bioplastic<sup>13</sup> with its production accounting for 18.9% of the entire bioplastics industry.<sup>14</sup> Its monomer, lactic acid, is currently prepared *via* the enzymatic fermentation of sugars, under strict temperature (< 313 K) and pH (5-7) conditions, followed by purification through subsequent esterification, distillation and hydrolysis (**Fig. 1a**).<sup>15,16</sup> Although this approach is used by 90% of the lactic acid manufacturers, its low productivity (1-13 g L<sup>-1</sup> h<sup>-1</sup>) and high production cost dictate the low annual growth rate for PLA. Perez-Ramirez and coworkers demonstrated an alternative approach where glycerol is first oxidised to dihydroxyacetone (DHA) and, in a separate batch, the DHA convert into lactic acid at 413 K and 25 bar.<sup>15</sup>

Glycerol electrolysis to lactic acid could potentially offer a more attractive, continuous route that avoids costs associated with the processing and purification of intermediates (**Fig. 1**). Further, being an anodic reaction, this process can be coupled with water reduction, for simultaneous hydrogen production, or other reduction reactions, e.g. CO<sub>2</sub> reduction, biomass-derived reduction reactions etc.<sup>7,17,18</sup> A recent life-cycle assessment demonstrated that electrocatalytic conversion of crude glycerol to lactic acid at 32% liquid product distribution and 100 kg/hr production rate can result in a 57% reduction in global warming potential compared to the bio- and chemocatalytic processes, when combined with a low-carbon-intensity grid.<sup>19</sup> Further emission reduction is possible when the product selectivity towards lactic acid is improved, pointing out the direction for further development. Reports of lactic acid electrosynthesis are limited, as listed in **Fig. 1b**.<sup>4</sup> In most of the cases, the glycerol electrolysis has been performed in a static half-cell configuration rather than a continuous membrane-electrode-assembly (MEA) electrolysis system. However, to maximize the benefits of coupling anode and cathode reactions, the set up must be compatible within a single system with easy product separation and high mass transport, in which case MEA electrolysis cell operating in galvanostatic mode holds greater promise in transferring the research into up-scaling devices than conventional H-cells.<sup>20</sup> Besides, to be industrial relevant, the process current density needs to be relatively high (i.e. > 200 mA cm<sup>-2</sup>),<sup>21-23</sup> and liquid product distribution towards lactic acid needs to exceed ~60 % to be compatible with the conventional fermentation method.<sup>24,25</sup> Reports falling into this area are rare. To date, only Yan et al. reported 80 % lactic acid selectivity in their recent works, yet the method for calculating the glycerol conversion rate and lactic acid selectivity need to be further validated to confirm the high selectivity.<sup>10,11</sup> Herein, based on the previous studies, we have chosen to perform our glycerol

electrolysis towards lactic acid and H<sub>2</sub> co-production in a MEA cell, with a reaction rate of 20 mA cm<sup>-2</sup>. Although the current density is a magnitude lower than practical industrial scale, the focus here is to achieve high lactic acid yield by designing the electrocatalyst structure and understanding the reaction mechanism. Engineering challenges towards scaling up will later be tackled with strategies such as constructing 3D electrode structure,<sup>26</sup> selecting suitable anion-exchange membrane,<sup>27,28</sup> and engineering the interface microenvironment,<sup>29–31</sup> taking inspiration from the electrochemical CO<sub>2</sub> reduction community.

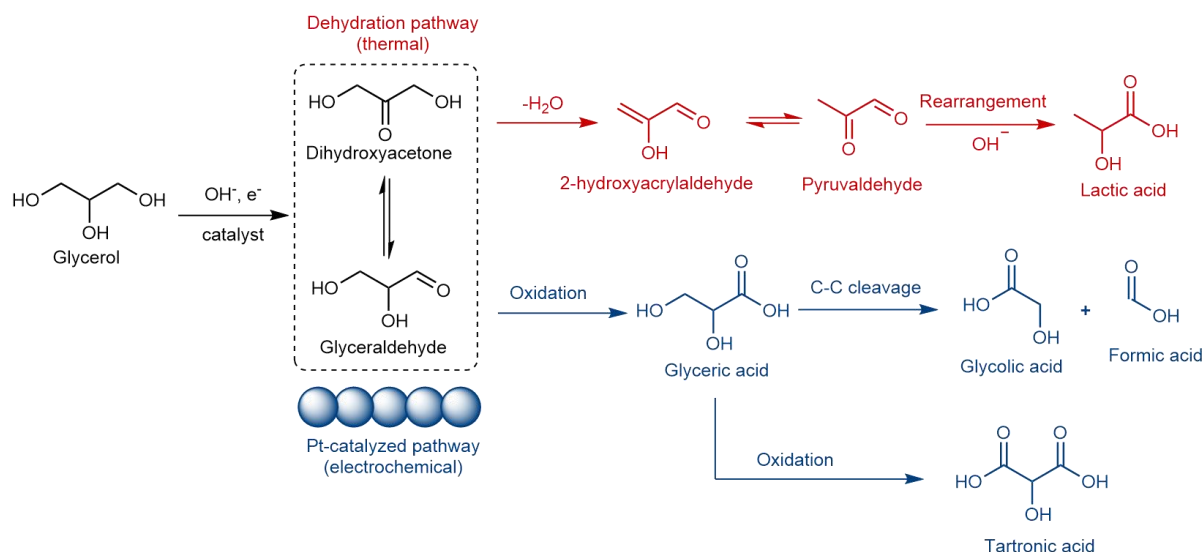


**Fig.2** | Glycerol dual reaction pathway: dehydration vs. oxidation. Pt based electrocatalysts can effectively catalyze the glycerol → DHA (dihydroxyacetone) / GLAD (glyceraldehyde) step as well as the following oxidation steps.<sup>12,32,33</sup>

Previous studies have shown that the glycerol to lactic acid transformation is a combination of electrochemical deprotonation – heterogeneous dehydration – homogeneous solution phase reaction process, with several intermediate steps involved, as illustrated in red (top) in **Fig. 2**.<sup>12,32,33</sup> Pt-based electrocatalysts are the most active in catalyzing the glycerol deprotonation step towards dihydroxyacetone and glyceraldehyde.<sup>34–37</sup> Density functional theory (DFT) calculations have already established the reaction pathways and the factors controlling activity and product selectivity within glycerol (electro-) oxidation on Pt(111) and other metal surfaces.<sup>38,39</sup> Subsequently, in a non-electrochemical solution phase step, it is possible to dehydrate DHA to lactic acid.<sup>40,41</sup> However, at oxidising potentials on Pt, the dehydration pathway towards lactic acid is less favoured than the competing electrochemical oxidation process towards glyceric acid (shown in blue (bottom) in **Fig. 2**).<sup>12,32,42</sup> Therefore, it is essential to develop an effective strategy to promote the dehydration pathway suppressing the electrochemical oxidation pathway within electrochemical glycerol oxidation.

In thermal (i.e. non electrochemical) heterogeneous catalysis, acidic sites from certain metal oxides, such as  $\text{TiO}_2$ ,<sup>43</sup>  $\text{ZrO}_2$ ,<sup>44</sup>  $\text{Al}_2\text{O}_3$ <sup>45</sup> and zeolites<sup>46–48</sup> can mediate the chemical transformation of DHA to pyruvaldehyde, by coordinating the carbonyl and hydroxyl groups, thus accelerating the keto-enol tautomerization and dehydration of the component.<sup>14</sup> When combined with metal catalysts, some metal oxides such as  $\text{TiO}_2$  can also directly convert glycerol into lactic acid, with the metal providing the dehydrogenation sites to produce DHA, and the transformation to lactic acid taking place on  $\text{TiO}_2$  surface.<sup>49</sup>

Taking inspiration from the abovementioned strategies from heterogeneous catalysis, in this paper, we aim to combine electrochemical experiments and DFT simulations to discover tandem electrocatalysts consisting of Pt and metal oxides for improving lactic acid product yield. We first examined the lactic acid product yield % on Pt/C catalyst standalone and employ DFT calculations to identify the reaction limitations. Subsequently, we screened a series of metal oxide materials with different acidic site densities, and designed a multicomponent tandem catalyst system containing Pt sites and metal oxides, to identify the experimental and theoretical descriptor for improving the product yield towards lactic acid leveraging further product optimization attempts.

## Results and Discussion

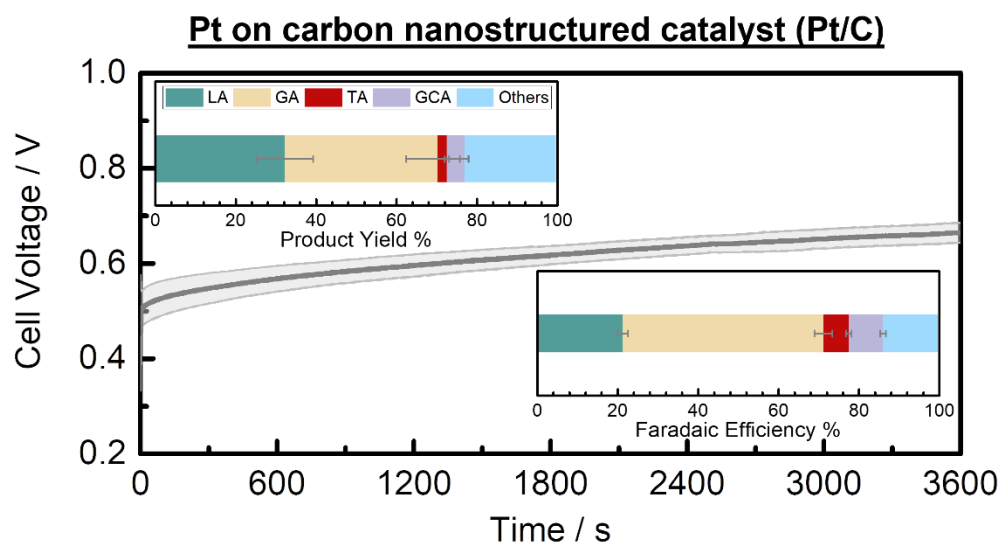


**Fig.3** | Electrolysis data showing the cell voltage change during 1 h experiment under  $20 \text{ mA cm}^{-2}$  applied current density. Inserts are the quantified products, defined as **Product Yield %**

$$= \frac{\text{product } X \text{ in mole}}{\text{consumed glycerol in mole}} \times 100\% \quad (\text{top}), \quad \text{and} \quad \text{Faradaic efficiency} =$$

$\frac{\text{mole of product formed} \times nF}{\text{total charge passed}} \times 100\%$  (bottom), where F is the Faradaic constant (96,485 C mol<sup>-1</sup>)

and n is the electron transfer number. Values are averaged from three independent measurements. The acronyms in this figure, **Fig. 4** and **Fig. 6** are: Gly: glycerol, GLAD: glyceraldehyde, GA: glyceric acid, TA: tartronic acid, GCA: glycolic acid, LA: lactic acid, FA: formic acid, DHA: dihydroxyacetone, 2-HAC: 2-hydroxyacrylaldehyde, PAH: pyruvaldehyde.

### Pure Pt catalysts lead to low lactic acid selectivity for glycerol electrooxidation.

The glycerol electrolysis was done with a commercial Pt on carbon nanostructured catalyst (Pt/C) mixed with SuperP carbon black (morphology and crystalline structures shown in **Fig. S1-S2**) using a MEA cell as described in the Methods Section. We show in **Fig. 3** that the Pt/C catalyst can generate lactic acid with a product yield of  $32.2 \pm 7\%$  and a Faradaic efficiency of  $21.2 \pm 1.3\%$  at a very low cell voltage of ca. 0.6 V. Glyceric acid was detected as the major product (product yield of  $38 \pm 8\%$  and Faradaic efficiency near 50%) and other compounds such as tartronic acid and glycolic acid were detected as minor products, likely formed *via* further oxidation of glyceric acid, as shown in **Fig. 2 and 3**. These results indicate that the standalone Pt/C catalyst cannot selectively catalyse the glycerol to lactic acid transformation with high efficiency, due to its high activity towards the competing electrochemical oxidation process.

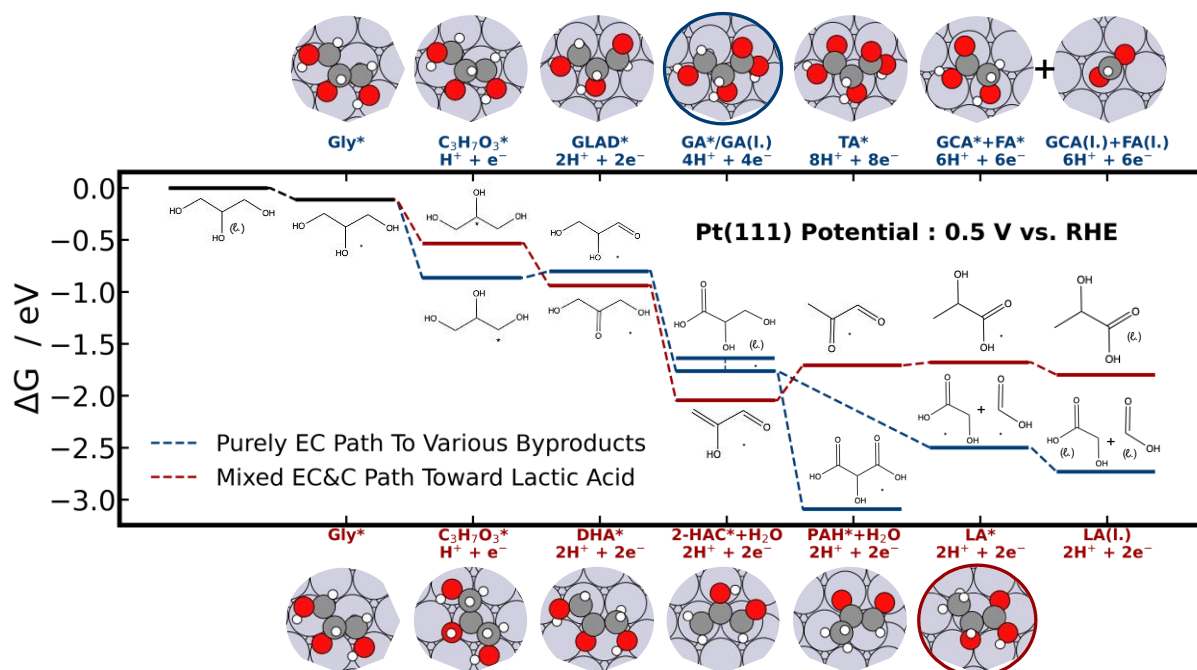


**Fig.4** | DFT-calculated free energy diagrams of the glycerol oxidation pathways outlined in **Fig. 2**, on Pt(111) at 0.5V vs. RHE. The blue line is the purely electrochemical (EC) path and the

red line is the Mixed electrochemical and chemical (EC&C) path. The related structures of different pathways are shown at the top and bottom of figure that the main product of purely EC is outlined in blue and the lactic acid is outlined in red. (l.): liquid phase, \*: adsorption at surface. More details on DFT results are in **SI: computational details**. Color codes for atoms: grey – platinum, white – hydrogen, red – oxygen, dark grey – carbon.

To rationalize the experimental observations on Pt above, we applied DFT to study the competition between the mixed electrochemical & chemical reaction path toward lactic acid and purely electrochemical (EC) pathways to the other products. We have simulated the Pt nanoparticle surfaces on the most stable (111) facet.<sup>50</sup> As shown in the free energy diagram in **Fig. 4**, we find that on a Pt (111) surface at 0.5 V vs. RHE, the most endergonic step of lactic acid production (shown in red in **Fig. 4**) is the chemical transformation of surface bound 2-hydroxyacrylaldehyde to pyruvaldehyde. On the contrary, the competing electrochemical pathway is virtually exergonic throughout (shown in blue in **Fig. 4**). The potential response of the latter pathway leads to a takeover of the product via the electrochemical path (shown in blue in **Fig. 2 and 4**) at increasing overpotentials. However, at low overpotential, the limiting potential for both pathways is determined by glycerol electro-oxidation to dihydroxyacetone (\*DHA) or glyceraldehyde (\*GLAD), respectively, with the formation of \*DHA being slightly preferred over \*GLAD. The free energy diagrams at different potentials are shown in **Fig. S3**. Besides, considering the pure electrochemical pathways, some elementary steps (outlined in **Fig. S4**) exhibit high limiting potentials, as shown in the free energy diagram in **Fig. S5a**, which inhibit the further production of tartronic acid and C-C splitting products at low overpotentials. However, the electrochemical reaction proceeds smoothly at 0.5V vs. RHE, as shown in **Fig. S5b**. Considering the reaction path toward lactic acid (red line in **Fig. 4**) at 0.5V vs. RHE, DHA as proton-electron transfer product is quite feasible and the following steps toward lactic acid are non-electrochemical which is potential independent. H Therefore, the low selectivity towards lactic acid on pure Pt surface can be attributed to a combination of limiting electrochemical activity towards DHA and GLAD at low overpotentials and the predominance of the electrochemical process even at moderate overpotentials. In order to increase lactic acid selectivity, engineering a catalytic system that promotes the dehydration route at moderate electrode potentials is thus required.

#### **Acidic sites on metal oxides steers lactic acid selectivity**

The identified limitations of Pt motivated us to explore new catalyst compositions favouring the non-electrochemical pathway, to improve lactic acid product yield. As mentioned above, previous studies have shown that metal oxides with surface acidic sites can facilitate the DHA to lactic acid transformation, where it is even possible to directly convert glycerol into lactic acid when combined with metal catalysts that drive the first deprotonation step.<sup>49</sup> Therefore, we screened several metal oxide materials with different acidic site densities, and designed a multicomponent tandem catalyst system containing Pt sites and metal oxides with abundant acidic sites, in order to combine the electrocatalytic capabilities of Pt to produce DHA from glycerol with the selectivity enhancement of the acid groups on the oxide towards lactic acid.

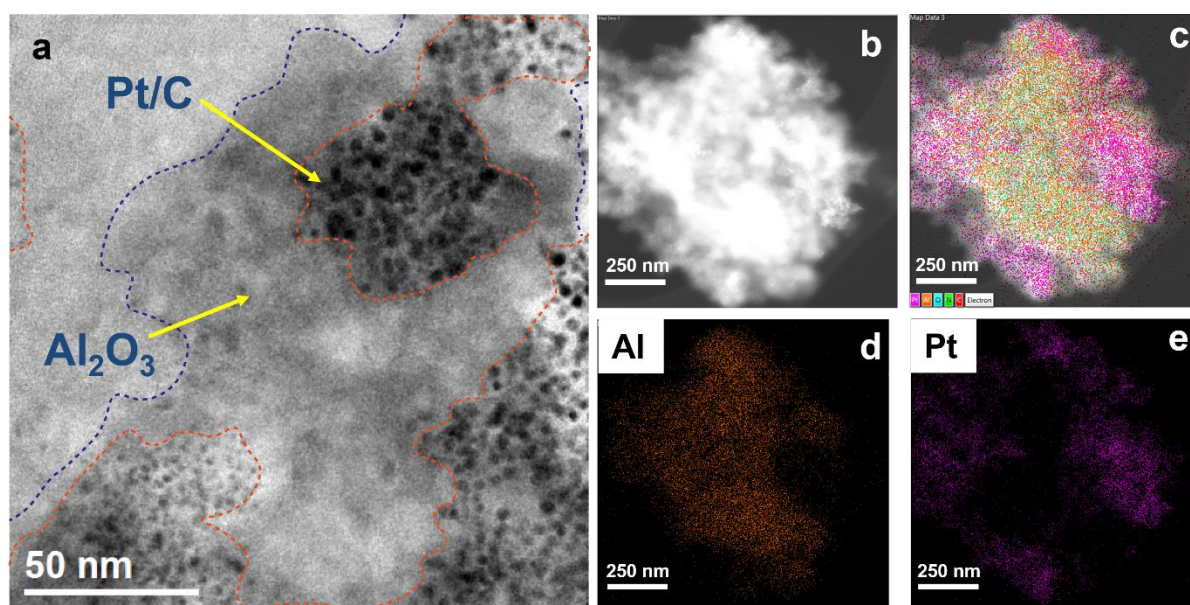


**Fig.5** | **a.** The morphology of Pt/C-Al<sub>2</sub>O<sub>3</sub> multicomponent catalyst: **a.** TEM image; **b-e:** STEM-EDS (**b:** HAADF-STEM, **c:** multi-element color mix; **d:** Al map; **e:** Pt map)

A series of metal oxides with different surface density of acidic sites were tested.<sup>51</sup> We fabricated the Pt/C-MO<sub>x</sub> (MO<sub>x</sub> (metal oxide) = CeO<sub>2</sub>, TiO<sub>2</sub> and  $\gamma$ -Al<sub>2</sub>O<sub>3</sub>) multicomponent electrodes by physically mixing commercial Pt/C (HiSPEC® 9100, Johnson & Matthey) and metal oxide nanopowders (Sigma Aldrich) and spray-coating on carbon paper support, as described previously for Pt/C. The mass ratio between Pt/C and metal oxides as well as the Pt loadings on all electrodes were kept equal as Pt/C, maintained at 1:3 ratio and Pt loading of 0.1 mg cm<sup>-2</sup>, respectively. The resulting morphology was characterized using electron microscopy, energy-dispersive X-ray spectroscopy (EDS) mapping and XRD. As shown in the TEM and EDS mappings (**Fig. 5 and S6**, in all Pt/C-MO<sub>x</sub> multicomponent systems, the metal oxide nanoparticles are intimately mixed at the nanoscale, providing good contact for charge and

mass transport. From the morphologies and XRD patterns (**Fig. S2**), it can be seen that  $\text{CeO}_2$  and  $\text{TiO}_2$  have a more crystalline structure, while  $\text{Al}_2\text{O}_3$  is more amorphous.<sup>52</sup> We have thus modelled both the most stable facets, i.e. fluorite- $\text{CeO}_2$  (111), anatase- $\text{TiO}_2$  (101) and  $\gamma$ - $\text{Al}_2\text{O}_3$  (111), and the more high surface energy (400) and (440) facets on  $\text{Al}_2\text{O}_3$ , as shown in **Fig. S7**.

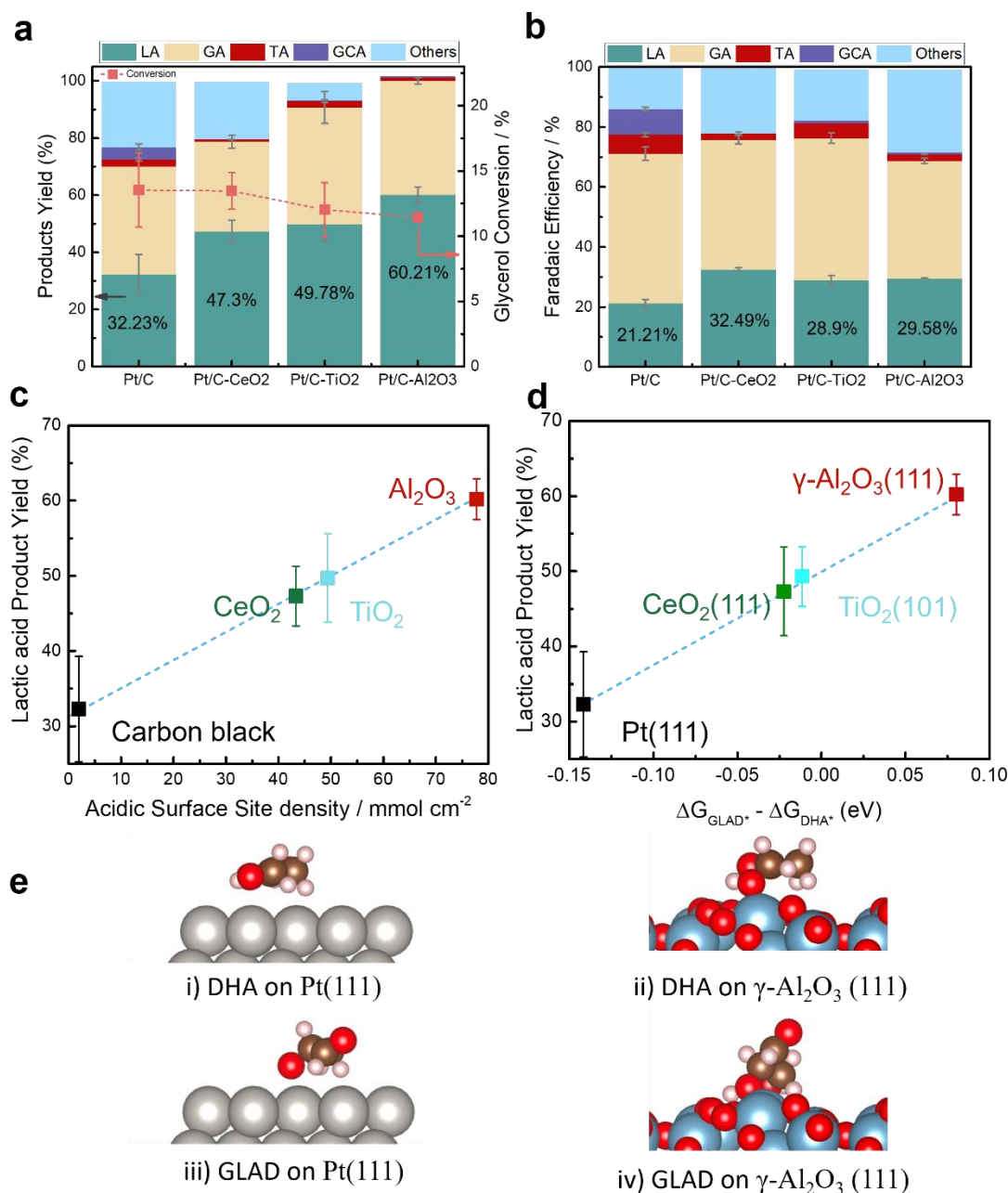


**Fig 6. a.** the product yield % and **b.** the faradaic efficiency for each product produced by Pt/C- $\text{MO}_x$  and Pt/C control. Values are averaged from three independent measurements. Current density:  $20 \text{ mA cm}^{-2}$ . Electrolysis duration: 1 h. The corresponding electrolysis data and HPLC chromatograph compound assignment are shown in **Fig. S8**. **c.** The correlation between lactic

acid / glycerol % and the acidic surface site density determined by NH<sub>3</sub>-TPD. **d.** the difference in adsorption free energy between GLAD and DHA as a descriptor of experimental results. **e.** the DHA and GLAD adsorption structure on i), iii) Pt(111) and on ii),iv)  $\gamma$ -Al<sub>2</sub>O<sub>3</sub>(111), respectively. The DFT calculation details and more structures are in **Fig S9-S10**. Color codes: red – oxygen, brown – carbon, silver– platinum, pink – hydrogen, blue – aluminum.

Electrolysis measurements applying Pt/C-MO<sub>x</sub> tandem catalysts were carried out under the same conditions as for the Pt/C. All the metal oxides and the carbon black features similar specific surface area (**Fig S11 and Table S1**), eliminating the effect from significant surface area differences.<sup>53</sup> **Fig 6a** shows the product yield % for each product produced by Pt/C-MO<sub>x</sub> and Pt/C control, with the Faradaic efficiency values of each product shown in **Fig 6b**. The results show that all Pt/C-MO<sub>x</sub> exhibit higher product yield towards lactic acid compared to the Pt/C control tested previously. In particular, for Pt/C-Al<sub>2</sub>O<sub>3</sub>, the lactic acid product yield % reached  $60.2 \pm 2.7$  %, nearly double that of the Pt/C standalone. Similar results can be seen from the Faradaic efficiency plot. Although the Faradaic efficiency towards glyceric acid is still higher than lactic acid, as producing the latter needs only half the number of the electrons, it is obvious that after adding the metal oxides, the partial current density towards lactic acid has significantly improved. The extended stability of the glycerol electrolysis process was evaluated using the Pt/C-Al<sub>2</sub>O<sub>3</sub> electrode. As shown in **Fig S12**, the glycerol electrolysis system exhibits a stable cell voltage below 1 V during 75 h of continuous operation at 20 mA cm<sup>-2</sup>, corresponding to an electricity consumption per unit of H<sub>2</sub> < 26 kWh kg<sup>-1</sup> H<sub>2</sub> (vs. ~38 kWh kg<sup>-1</sup> H<sub>2</sub> for alkaline water electrolyser at similar current density),<sup>28</sup> while the lactic acid product yield is maintained above 35 %.

To further validate whether the acidic sites on the metal oxide surfaces play a role, NH<sub>3</sub> temperature programmed desorption (NH<sub>3</sub>-TPD) was used to determine the total acidic site concentration and relative strength of the metal oxide catalysts. The data profile is presented in **Fig S13**, and the acidity of all metal oxides was calculated by integrating the area under the profile curve normalised by the mass of the catalyst. As a benchmark, the surface acidity of pure carbon black was also measured. The values are summarized in **Table S1**. As **Fig. 6c** shows, we identified a linear relationship between the lactic acid product yield values and acidic site density of different metal oxides

DFT calculations were performed to further elucidate why the addition of metal oxides enhances the product yield towards lactic acid by studying the adsorption of reaction intermediates on the metal oxides with respect to Pt. We explored the trend in DHA and GLAD adsorption, the key precursors of the competing reaction pathways, against lactic acid product yield of all catalysts.

We identified that the free energies of both DHA and GLAD intermediates adsorption scale linearly with  $\text{NH}_3$  adsorption, our probe to titrate the number of acidic sites (cf. **Fig S14**). Thus, merely increasing the acidic site activity does not fully explain the improved lactic acid yield. The relative adsorption strength of the two key intermediates, on the other hand, shows a clear trend reflecting the identified selectivity behaviour, with experimental lactic acid product yield % correlates linearly with  $(\Delta G_{\text{GLAD}^*} - \Delta G_{\text{DHA}^*})$  (**Fig. 6d**). We interpret the increase in  $(\Delta G_{\text{GLAD}^*} - \Delta G_{\text{DHA}^*})$  as the ability of the materials in adsorbing DHA, the precursor of lactic acid, over GLAD and to induce dehydration on metal oxide catalysts. Pure Pt preferably binds GLAD over DHA, while  $\text{TiO}_2$  and  $\text{CeO}_2$  adsorb both intermediates with comparable strength and  $\gamma\text{-Al}_2\text{O}_3$  binds DHA stronger. To understand this selectivity descriptor in more detail, we highlight the binding configurations of DHA and GLAD on Pt and  $\text{Al}_2\text{O}_3$  in **Fig. 6e**. GLAD tends to chemisorb *via* its central OH-group on both surfaces. DHA on the other hand is only physisorbed in a flat configuration on Pt, while being chemisorbed *via* its terminal OH-group on the acidic site of  $\text{Al}_2\text{O}_3$ . An analogous chemisorbed binding configuration of DHA has been identified on the other studied metal oxide catalysts, as shown in **Fig S9**. Thus, we conclude that while both GLAD and DHA benefit from the acidity of the catalyst binding sites, the chemisorption of DHA on metal oxide catalysts is the primary cause in the increase in selectivity and product yield towards lactic acid.

## Conclusion

In this work, we have developed a MEA-based tandem catalytic system to boost lactic acid yield *via* glycerol electrooxidation. The high lactic acid product yield of 60.2 % (64% if calculated as liquid product distribution towards lactic acid) at a current density of  $20 \text{ mA cm}^{-2}$  was achieved with a Pt/C- $\gamma\text{-Al}_2\text{O}_3$  multicomponent catalyst that nearly doubled that of Pt/C standalone catalyst. Combining  $\text{NH}_3$ -TPD experiment and theoretical calculations, we demonstrated that the improved yield towards lactic acid is attributed to the high density of surface acidic sites provided by the  $\gamma\text{-Al}_2\text{O}_3$  and their strong binding to DHA intermediate, a precursor relevant for the dehydration pathway towards lactic acid, thus preventing further

electrochemical oxidation on Pt.  $\Delta G_{GLAD}^* - \Delta G_{DHA}^*$ , defined as adsorption energy difference between DHA and GLAD, is derived as the selectivity descriptor, which showed linear relationship to the lactic acid product yield %. Our finding suggests that an increased difference in the adsorption free energy of the key precursors of the competing reaction pathways should be screened for when searching for high selectivity toward lactic acid under moderate electrode potential. Although the research in this field is still at early stage, with current density a magnitude lower than practical industrial scale, the insights gained from this work may bring inspirations to design other electrochemical oxidation reactions for high-value commodity chemical production, facilitating the decarbonisation of the chemical industry. Strategies such as constructing 3D electrode structure, selecting suitable anion-exchange membrane, and engineering the interface microenvironment may be deployed to solve the engineering challenges towards scaling up.

## Methods

**Preparation of electrodes.** The anodes were prepared by mixing 3 mg Pt/C 60% catalysts (HiSPEC® 9100, Johnson & Matthey), 9 mg Super P® carbon black (Alfa Aesar) or metal oxides (CeO<sub>2</sub>, TiO<sub>2</sub> or  $\gamma$ -Al<sub>2</sub>O<sub>3</sub> (Sigma-Aldrich), 1584  $\mu$ L ethanol, 4200  $\mu$ L H<sub>2</sub>O, and 216  $\mu$ L Nafion solution (5% w/w). The mixture was then sonicated for 10 min with probe ultrasonicator to obtain a homogeneous slurry. 3 mL of the slurry was spray coated onto 3\*3 cm<sup>2</sup> carbon fiber paper (Freudenberg H23, Fuel Cell Store) to achieve a Pt loading of 0.1 mg cm<sup>-2</sup>. The cathode used in this reaction was also Pt/C 60% catalyst, prepared with the same spray coating method with a Pt loading of 0.05 mg cm<sup>-2</sup>. The prepared electrodes were then placed in a vacuum oven and dried at 60 °C overnight.

**Characterization.** HR-TEM images and EDS mappings were obtained by a JOEL-2100F electron microscope at an operating voltage of 200 kV. LEO Gemini 1525 FEGSEM were used for SEM imaging. The XRD patterns were performed using PANalytical's X'PERTPRO X-ray diffractometer with Ni filtered Cu K $\alpha$  radiation and an X'Celerator multistrip detector. N<sub>2</sub> sorption isotherms were conducted at -196 °C with data collected from pressure range 10<sup>-5</sup> to 0.99 in Micromeritics 3Flex system with ~10 mg of degassed sample (200 °C overnight). NH<sub>3</sub>-TPD measurements were performed on a homemade system formed by a mass flow controllers (MFC) equipped with a horizontal tube furnace where the sample is placed, connected with an Agilent Technologies 7820A Gas Chromatograph equipped with a thermal conductivity detector. Each analysis was performed packing ~100 mg of sample into a ¼" quartz tube,

using two plugs of quartz wool to hold the sample in the center of the tube, which was then placed inside a tubular furnace. Samples were pre-treated in He flow (22.7 mL/min) at 400 °C for 1h (ramp rate 10 °C/min) to remove species initially adsorbed on the surface. NH<sub>3</sub> was subsequently adsorbed on to the samples by flowing 0.5 mol % NH<sub>3</sub> in He over the sample for 30 minutes at 30 °C at a flow of 38.6 mL/min. Subsequently, the sample was purged in He flow (29.4 mL/min) for 45 minutes at 30 °C to remove excess physisorbed NH<sub>3</sub>. NH<sub>3</sub> desorption profiles were collected in He flow (22 mL/min) using the following program: i) 10 minutes isotherm at 30 °C, ii) heating to 400 °C with a ramp rate of 10 °C/min.

**Glycerol electrolysis.** Commercial Pt/C 60 wt% catalyst was first used to test the glycerol electrolysis towards lactic acid with a Metrohm Autolab PGSTAT204 potentiostat. Electrolysis measurements were carried out using an alkaline anion exchange membrane (AEM) electrolyser cell (Dioxide Materials SKU: 68731) with 5 cm<sup>2</sup> geometric surface area. Measurement was done under galvanostatic mode, with constant applied current of 100 mA (20 mA cm<sup>-2</sup>). The above-mentioned electrodes were used as anodes and cathodes, and the anion-exchange membrane is Fumasep FAA-3-50 (fumatech). Experiments were performed for 1 hour with 1 M glycerol/1 M NaOH as anolyte and 1 M NaOH as catholyte, circulated through the MEA bipolar plate flow channels from the respective electrolyte reservoirs using a dual-channel peristaltic pump (JIHPUMP BT-EA-50) at 50 rpm flow rate. N<sub>2</sub> (Zero Grade, BOC) was used as purging gas to the electrolyte reservoirs to maintain an inert atmosphere. The cell temperature was maintained at 60 °C. At the end of the experiments, the anolyte and catholyte in the anode and cathode chambers were sampled and quantified with high performance liquid chromatography (HPLC) respectively. The specific HPLC method used and product analysis <sup>54</sup>

**Computational methods.** DFT calculations were performed by using the Vienna Ab Initio Software Package (VASP)<sup>55</sup> employing the projector-augmented wave method.<sup>56</sup> Valence electrons were described with plane waves with cutoff energy up to 500 eV. Methfessel-Paxton smearing with width of 0.2 eV was used. We applied RPBE<sup>57</sup> functional and the dispersion correction with Grimme D3<sup>58</sup> method. Monkhorst-Pack grids<sup>59</sup> with dimensions of 3x3x1 or 3x4x1, which depends on the surface slab symmetry, were used to sample the Brillouin zone to calculate adsorption energy. The molecular structure of the adsorbates used in the adsorption energy calculation are listed in **Fig. S15**. The bottom two layers were fixed in the bulk structure whereas the upper layers and adsorbates were allowed to relax in all directions until residual forces were less than 0.01 eV Å<sup>-1</sup>. Vibrational frequencies of adsorbates were computed using

a finite difference method as implemented in VASP (IBRION = 5). For surface Pourbaix Diagram, we used a smaller surface structure to calculate the O\* and OH\* adsorption phase under different coverage by sampling the surface sites (**Fig.S16-S18**). The computational hydrogen electrode (CHE)<sup>60</sup> was used to calculate the electrode potential dependent reaction energy with proton-electron transfer in the reactant. For convenient handling of all atomic structures, the Atomic Simulation Environment (ASE)<sup>61</sup> was used. Further details on DFT calculations are provided in SI Part.7. All computational data, including the adsorption energy of glycerol and each key intermediates, Pourbaix diagram, vibrational calculations, and python analysis scripts are available at [https://github.com/CatTheoryDTU/Glycerol\\_To\\_LacticAcid](https://github.com/CatTheoryDTU/Glycerol_To_LacticAcid).

## Data Availability

The data that support the findings of this study are available within the main text and the Supplementary Information file. Source data can be found here: <https://doi.org/10.6084/m9.figshare.25024544>. Data are also available from the corresponding author upon request.

## Acknowledgements

The work was supported by a donation from Mr Mark Richardson to the Department of Chemical Engineering at Imperial College London. MX and SL were supported by research grant no. 29450 from Villum Fonden. GK was supported by grant no. 9455, V-Sustain, from Villum Fonden. HY and AYL acknowledges Marie Skłodowska-Curie Individual European Fellowship. CH thanks the support from the Royal Society University Research Fellowship under URF\R\201003 and RF\ERE\210203. IELS acknowledges funding from acknowledges funding from the European Research Council (ERC) under the European Union's Horizon 2020 research and innovation programme (grant agreement no. 866402). MT acknowledges funding from the Royal Academy of Engineering Chair in Emerging Technologies.

## Authorship Inclusion & Ethics

The authors declare no competing interests.

All the experimental part of research is conducted locally within the same UK institution by local researchers, while theoretical part is done by collaboration with experts in a foreign institution. Roles and responsibilities were agreed amongst collaborators ahead of the research. We have taken local and regional research relevant to our study into account in citations.

## Author Contribution Statement

H.L., K.C., G.K., I.E.L.S., M.M.T conceived and designed the experiments. H.L., G.T., H.Y., A.Y.L performed the experiments. M.X., S.L., G.K. performed the DFT calculations. H.L.,

M.X., S.L., G.T., C.H. analysed the data. H.L., M.X., S.L., A.Y.L., G.K., I.E.L.S, M.M.T. co-wrote the paper. All the authors discussed the results and reviewed the manuscript.

1. International Energy Agency (IEA). Chemicals. (2021).
2. Levi, P. G. & Cullen, J. M. Mapping Global Flows of Chemicals : From Fossil Fuel Feedstocks to Chemical Products. *Environ Sci Technol* **52**, 1725–1734 (2018).
3. European Commission. *A sustainable bioeconomy for Europe : strengthening the connection between economy , society and the environment*. (2018) doi:10.2777/478385.
4. Lam, C. H., Bloomfield, A. J. & Anastas, P. T. A switchable route to valuable commodity chemicals from glycerol via electrocatalytic oxidation with an earth abundant metal oxidation catalyst. *Green Chemistry* **19**, 1958–1968 (2017).
5. Zhou, Y., Shen, Y. & Xi, J. Seed-mediated synthesis of Pt<sub>x</sub>Au<sub>y</sub>@Ag electrocatalysts for the selective oxidation of glycerol. *Appl Catal B* **245**, 604–612 (2019).
6. Lee, C. S. *et al.* Selective electrochemical conversion of glycerol to glycolic acid and lactic acid on a mixed carbon-black activated carbon electrode in a single compartment electrochemical cell. *Front Chem* **7**, 1–11 (2019).
7. Yadegari, H. *et al.* Glycerol Oxidation Pairs with Carbon Monoxide Reduction for Low-Voltage Generation of C<sub>2</sub> and C<sub>3</sub> Product Streams. *ACS Energy Lett* **6**, 3538–3544 (2021).
8. Houache, M. S. E., Hughes, K., Safari, R., Botton, G. A. & Baranova, E. A. Modification of Nickel Surfaces by Bismuth: Effect on Electrochemical Activity and Selectivity toward Glycerol. *ACS Appl Mater Interfaces* **12**, 15095–15107 (2020).
9. Kim, D. *et al.* Enhancing Glycerol Conversion and Selectivity toward Glycolic Acid via Precise Nanostructuring of Electrocatalysts. *ACS Catal* **11**, 14926–14931 (2021).
10. Yan, Y. *et al.* Photoassisted Strategy to Promote Glycerol Electrooxidation to Lactic Acid Coupled with Hydrogen Production. *ACS Appl Mater Interfaces* **15**, 23265–23275 (2023).
11. Yan, Y. *et al.* Electrocatalytic Upcycling of Biomass and Plastic Wastes to Biodegradable Polymer Monomers and Hydrogen Fuel at High Current Densities. *J Am Chem Soc* **145**, 6144–6155 (2023).
12. Dai, C. *et al.* Electrochemical production of lactic acid from glycerol oxidation catalyzed by AuPt nanoparticles. *J Catal* **356**, 14–21 (2017).
13. Magdalena Zaborowska, K. B. The development of recycling methods for bio-based materials – A challenge in the implementation of a circular economy: A review. *Waste Management & Research* 1–13 (2022) doi:10.1177/0734242X221105432.
14. Iglesias, J. *et al.* Advances in catalytic routes for the production of carboxylic acids from biomass: A step forward for sustainable polymers. *Chem Soc Rev* **49**, 5704–5771 (2020).
15. Morales, M. *et al.* Environmental and economic assessment of lactic acid production from glycerol using cascade bio- and chemocatalysis. *Energy Environ Sci* **8**, 558–567 (2015).
16. Lari, G. M. *et al.* Environmental and economical perspectives of a glycerol biorefinery. *Energy Environ Sci* **11**, 1012–1029 (2018).
17. Luo, H. *et al.* Progress and Perspectives in Photo- and Electrochemical-Oxidation of Biomass for Sustainable Chemicals and Hydrogen Production. *Adv Energy Mater* 2101180 (2021) doi:10.1002/aenm.202101180.
18. Verma, S., Lu, S. & Kenis, P. J. A. Co-electrolysis of CO<sub>2</sub> and glycerol as a pathway to carbon chemicals with improved techno-economics due to low electricity consumption. *Nat Energy* **4**, 466–474 (2019).
19. Tu, Q. *et al.* Electrocatalysis for chemical and fuel production: Investigating climate change mitigation potential and economic feasibility. *Environ Sci Technol* **55**, 3240–3249 (2021).
20. Cheon, S., Kim, W. J., Kim, D. Y., Kwon, Y. & Han, J. I. Electro-synthesis of Ammonia from Dilute Nitric Oxide on a Gas Diffusion Electrode. *ACS Energy Lett* **7**, 958–965 (2022).
21. Ehlers, J. C., Feidenhans'l, A. A., Therkildsen, K. T. & Larrazábal, G. O. Affordable Green Hydrogen from Alkaline Water Electrolysis: Key Research Needs from an Industrial Perspective. *ACS Energy Letters* vol. 8 1502–1509 Preprint at <https://doi.org/10.1021/acsenerylett.2c02897> (2023).

22. De Luna, P. *et al.* What would it take for renewably powered electrosynthesis to displace petrochemical processes? *Science* vol. 364 Preprint at <https://doi.org/10.1126/science.aav3506> (2019).
23. Segets, D., Andronesco, C. & Apfel, U. P. Accelerating CO<sub>2</sub> electrochemical conversion towards industrial implementation. *Nat Commun* **14**, 7950 (2023).
24. Bonk, F., Bastidas-Oyanedel, J. R., Yousef, A. F., Schmidt, J. E. & Bonk, F. Exploring the selective lactic acid production from food waste in uncontrolled pH mixed culture fermentations using different reactor configurations. *Bioresour Technol* **238**, 416–424 (2017).
25. Wang, Y. *et al.* Chemical synthesis of lactic acid from cellulose catalysed by lead(II) ions in water. *Nat Commun* **4**, (2013).
26. Suter, S. & Haussener, S. Optimizing mesostructured silver catalysts for selective carbon dioxide conversion into fuels. *Energy Environ Sci* **12**, 1668–1678 (2019).
27. Giron Rodriguez, C. A. *et al.* Influence of Headgroups in Ethylene-Tetrafluoroethylene-Based Radiation-Grafted Anion Exchange Membranes for CO<sub>2</sub> Electrolysis. *ACS Sustain Chem Eng* **11**, 1508–1517 (2023).
28. Liu, Z. *et al.* The effect of membrane on an alkaline water electrolyzer. *Int J Hydrogen Energy* **42**, 29661–29665 (2017).
29. Lum, Y. & Ager, J. W. Sequential catalysis controls selectivity in electrochemical CO<sub>2</sub> reduction on Cu. *Energy Environ Sci* **11**, 2935–2944 (2018).
30. Gu, J. *et al.* Modulating electric field distribution by alkali cations for CO<sub>2</sub> electroreduction in strongly acidic medium. *Nat Catal* **5**, 268–276 (2022).
31. Pelayo García de Arquer, F. *et al.* CO<sub>2</sub> electrolysis to multicarbon products at activities greater than 1 A cm<sup>-2</sup>. <https://www.science.org>.
32. Purushothaman, R. K. P. *et al.* An efficient one pot conversion of glycerol to lactic acid using bimetallic gold-platinum catalysts on a nanocrystalline CeO<sub>2</sub> support. *Appl Catal B* **147**, 92–100 (2014).
33. Brix, A. C. *et al.* Electrocatalytic Oxidation of Glycerol Using Solid-State Synthesised Nickel Boride: Impact of Key Electrolysis Parameters on Product Selectivity. *ChemElectroChem* **8**, 2336–2342 (2021).
34. Li, T. & Harrington, David. Overview of glycerol electrooxidation mechanisms on Pt, Pd and Au. *ChemSusChem* **14**, 1472–1495 (2021).
35. Yu, Z., Yue, X., Fan, J. & Xiang, Q. Crystalline Intramolecular Ternary Carbon Nitride Homojunction for Photocatalytic Hydrogen Evolution. *ACS Catal* **12**, 6345–6358 (2022).
36. Valter, M., Dos Santos, E. C., Pettersson, L. G. M. & Hellman, A. Selectivity of the first two glycerol dehydrogenation steps determined using scaling relationships. *ACS Catal* **11**, 3487–3497 (2021).
37. Valter, M. *et al.* Electrooxidation of Glycerol on Gold in Acidic Medium: A Combined Experimental and DFT Study. *Journal of Physical Chemistry C* **122**, 10489–10494 (2018).
38. Liu, B. & Greeley, J. Decomposition Pathways of Glycerol via C–H, O–H, and C–C Bond Scission on Pt(111): A Density Functional Theory Study. *The Journal of Physical Chemistry C* **115**, 19702–19709 (2011).
39. Valter, M., dos Santos, E. C., Pettersson, L. G. M. & Hellman, A. Partial Electrooxidation of Glycerol on Close-Packed Transition Metal Surfaces: Insights from First-Principles Calculations. *The Journal of Physical Chemistry C* **124**, 17907–17915 (2020).
40. Liu, B. & Greeley, J. Decomposition pathways of glycerol via C-H, O-H, and C-C bond scission on Pt(111): A density functional theory study. *Journal of Physical Chemistry C* **115**, 19702–19709 (2011).
41. Yan, H. *et al.* Selective oxidation of glycerol to carboxylic acids on Pt(111) in base-free medium: A periodic density functional theory investigation. *Appl Surf Sci* **497**, 143661 (2019).
42. Shen, Y., Zhang, S., Li, H., Ren, Y. & Liu, H. Efficient synthesis of lactic acid by aerobic oxidation of glycerol on Au-Pt/TiO<sub>2</sub> catalysts. *Chemistry - A European Journal* **16**, 7368–7371 (2010).
43. Santos, K. M. A., Albuquerque, E. M., Borges, L. E. P. & Fraga, M. A. Discussing Lewis and Brønsted acidity on continuous pyruvaldehyde Cannizzaro reaction to lactic acid over solid catalysts. *Molecular Catalysis* **458**, 198–205 (2018).

44. Albuquerque, E. M., Borges, L. E. P., Fraga, M. A. & Sievers, C. Relationship between Acid–Base Properties and the Activity of ZrO<sub>2</sub>-Based Catalysts for the Cannizzaro Reaction of Pyruvaldehyde to Lactic Acid. *ChemCatChem* **9**, 2675–2683 (2017).
45. Albuquerque, E. M., Borges, L. E. P. & Fraga, M. A. Lactic acid production from aqueous-phase selective oxidation of hydroxyacetone. *J Mol Catal A Chem* **400**, 64–70 (2015).
46. Holm, M. S., Saravanamurugan, S. & Taarning, E. Conversion of Sugars to Lactic Acid Derivatives Using Heterogeneous Zeotype Catalysts. *Science (1979)* **328**, 602–605 (2010).
47. Pescarmona, P. P. *et al.* Zeolite-catalysed conversion of C<sub>3</sub> sugars to alkyl lactates. *Green Chemistry* **12**, 1083–1089 (2010).
48. West, R. M. *et al.* Zeolite H-USY for the production of lactic acid and methyl lactate from C<sub>3</sub>-sugars. *J Catal* **269**, 122–130 (2010).
49. Chu, D., Zhou, H. & Luo, Z. CrO<sub>x</sub> decoration on Fe/TiO<sub>2</sub> with tunable and stable oxygen vacancies for selective oxidation of glycerol to lactic acid. *New Journal of Chemistry* **46**, 18744–18750 (2022).
50. Vitos, L., Ruban, A. V, Skriver, H. L. & Kollár, J. *The surface energy of metals*. *Surface Science* vol. 411 (1998).
51. Shimizu, K. I., Kon, K., Shimura, K. & Hakim, S. S. M. A. Acceptor-free dehydrogenation of secondary alcohols by heterogeneous cooperative catalysis between Ni nanoparticles and acid-base sites of alumina supports. *J Catal* **300**, 242–250 (2013).
52. Gu, J., Wang, J. & Leszczynski, J. Structure and Energetics of (111) Surface of  $\gamma$ -Al<sub>2</sub>O<sub>3</sub>: Insights from DFT Including Periodic Boundary Approach. *ACS Omega* **3**, 1881–1888 (2018).
53. Chen, C. *et al.* Cu–Ag Tandem Catalysts for High-Rate CO<sub>2</sub> Electrolysis toward Multicarbon. *Joule* **4**, 1688–1699 (2020).
54. Luo, H. *et al.* Role of Ni in PtNi Bimetallic Electrocatalysts for Hydrogen and Value-Added Chemicals Coproduction via Glycerol Electrooxidation. *ACS Catal* 14492–14506 (2022) doi:10.1021/acscatal.2c03907.
55. Kresse, G. & Furthmüller, J. Efficient iterative schemes for ab initio total-energy calculations using a plane-wave basis set. *Phys Rev B* **54**, 11169–11186 (1996).
56. Kresse, G. & Joubert, D. From ultrasoft pseudopotentials to the projector augmented-wave method. *Phys Rev B* **59**, 1758–1775 (1999).
57. Hammer, B., Hansen, L. B. & Nørskov, J. K. Improved adsorption energetics within density-functional theory using revised Perdew–Burke–Ernzerhof functionals. *Phys Rev B* **59**, 7413–7421 (1999).
58. Grimme, S., Antony, J., Ehrlich, S. & Krieg, H. A consistent and accurate ab initio parametrization of density functional dispersion correction (DFT–D) for the 94 elements H–Pu. *J Chem Phys* **132**, 154104 (2010).
59. Monkhorst, H. J. & Pack, J. D. Special points for Brillouin-zone integrations. *Phys Rev B* **13**, 5188–5192 (1976).
60. Nørskov, J. K. *et al.* Origin of the overpotential for oxygen reduction at a fuel-cell cathode. *Journal of Physical Chemistry B* **108**, 17886–17892 (2004).
61. Hjorth Larsen, A. *et al.* The atomic simulation environment—a Python library for working with atoms. *Journal of Physics: Condensed Matter* **29**, 273002 (2017).

Supporting Information of

## **Selective glycerol to lactic acid conversion via a tandem effect between platinum and metal oxides with abundant acid groups**

Hui Luo,<sup>1,2†</sup> Mianle Xu,<sup>3†</sup> Sihang Liu,<sup>3</sup> Giulia Tarantino,<sup>1</sup> Hossein Yadegari,<sup>4</sup> Alain Y. Li,<sup>1</sup> Karen Chan,<sup>3</sup> Ceri Hammond,<sup>1</sup> Georg Kastlunger,<sup>3\*</sup> Ifan E. L. Stephens,<sup>4\*</sup> Maria-Magdalena Titirici<sup>1\*</sup>

### **Table of Contents**

<b>1) Catalyst Surface Characterization</b>	<b>2</b>
a. 19	
b. 19	
<b>2) Free Energy Diagram under different conditions</b>	<b>2</b>
<b>3) Surface Structures and Modelling</b>	<b>5</b>
a. 22	
b. 22	
<b>4) Electrolysis Data</b>	<b>7</b>
<b>5) DFT Structures: Relaxed Adsorption Structures</b>	<b>8</b>
<b>6) Surface Acidity and Adsorption Free Energy</b>	<b>10</b>
a. 27	
b. 27	
c. 28	
<b>7) Computational details</b>	<b>11</b>
a. 29	
b. 29	
c. 30	
d. 34	
e. 36	

## 1) Catalyst Surface Characterization

### a. Catalyst morphology (Pt)

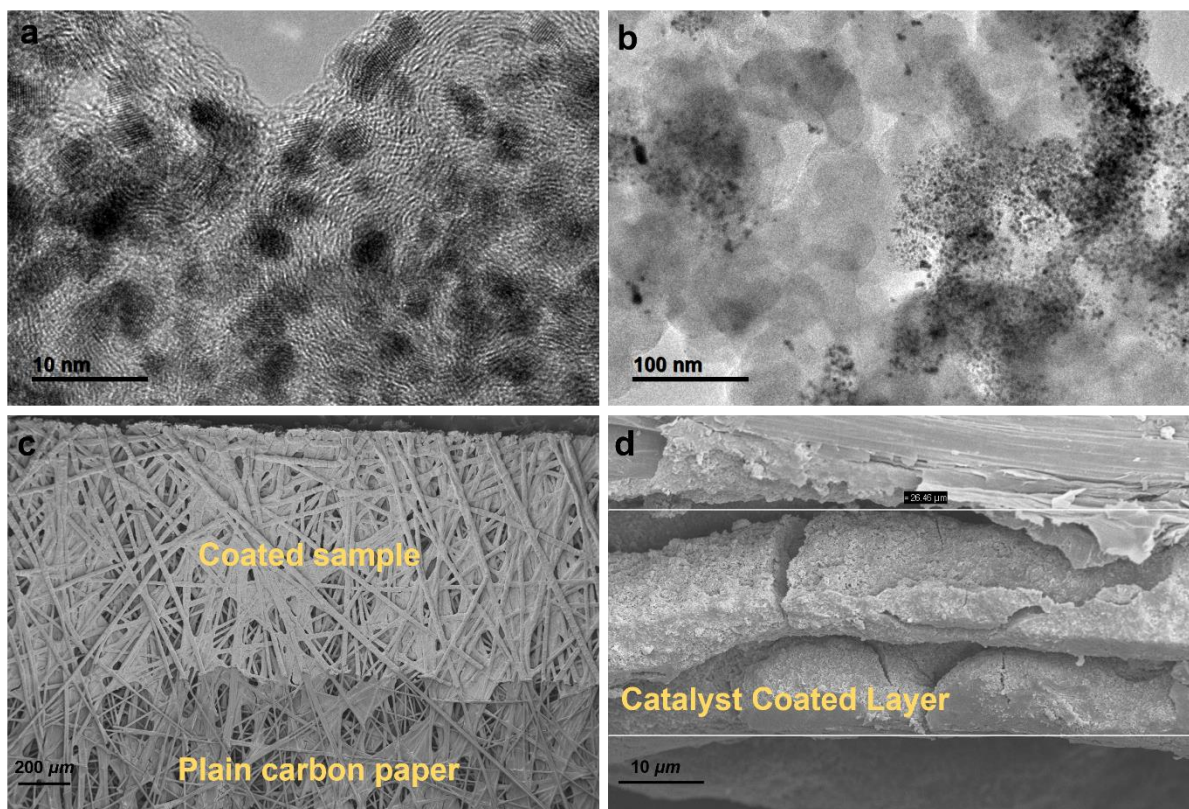


Figure S1. Pt/C catalyst and electrode morphology. *a* and *b*. The morphology of the Pt/C catalyst was first investigated with transmission electron microscopy (TEM). The Pt/C nanoparticles have a diameter of 3-5 nm, and in close contact with the carbon black substrate. *c* and *d*. are the scanning electron microscopy (SEM) images of the Pt/C coated carbon paper electrode. After coating, the electrode colour changed slightly, and the catalyst coated layer is approximately 26.5  $\mu\text{m}$  in thickness.

### b. Catalysts structure by XRD

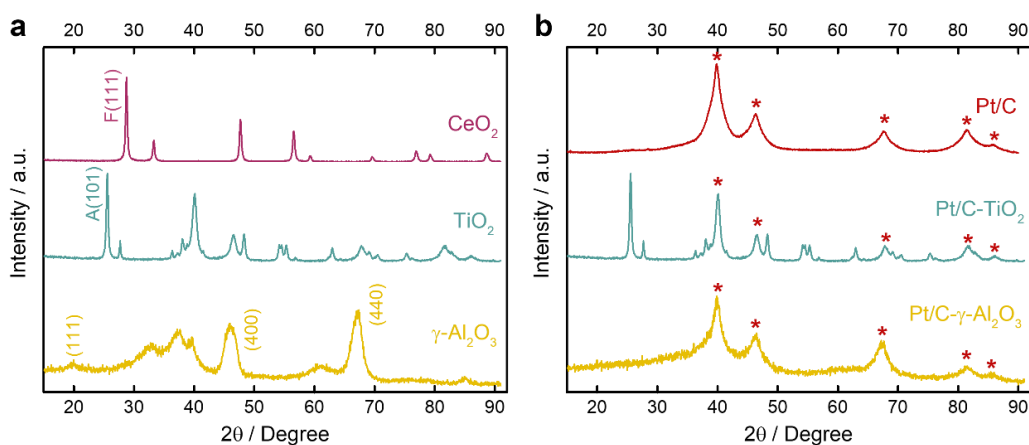


Figure S2. Pt/C- $\text{MO}_x$  multicomponent catalysts structure. *a*: XRD for three different kinds of metal oxides; *b*: XRD for Pt/C, Pt/C- $\text{TiO}_2$ , Pt/C- $\gamma\text{-Al}_2\text{O}_3$

## 2) Free Energy Diagram (FED) under different conditions

The FEDs are key to understanding the reaction and selectivity, to match the experimental condition and how the electrode potential affects the selectivity. We plotted several FEDs under different potential. The free energy was calculated from the method introduced in part 5.

At the beginning, we plotted the dual pathway FEDs in 0V and 0.5V vs. RHE. The FEDs plots are shown in Figure S3 and Fig.4. In these plots, electrode potential is an important parameter in tuning the dual pathway as well as selectivity, just mentioned in the main text.

Considering the continuous electrode chemical process, as a competitive pathway toward lactic acid, the elementary proton-electron transfer has been calculated to understand the electrochemical products distribution. The plots in different electrode potentials in 0V and 0.5V vs. RHE are shown in Figure S4.

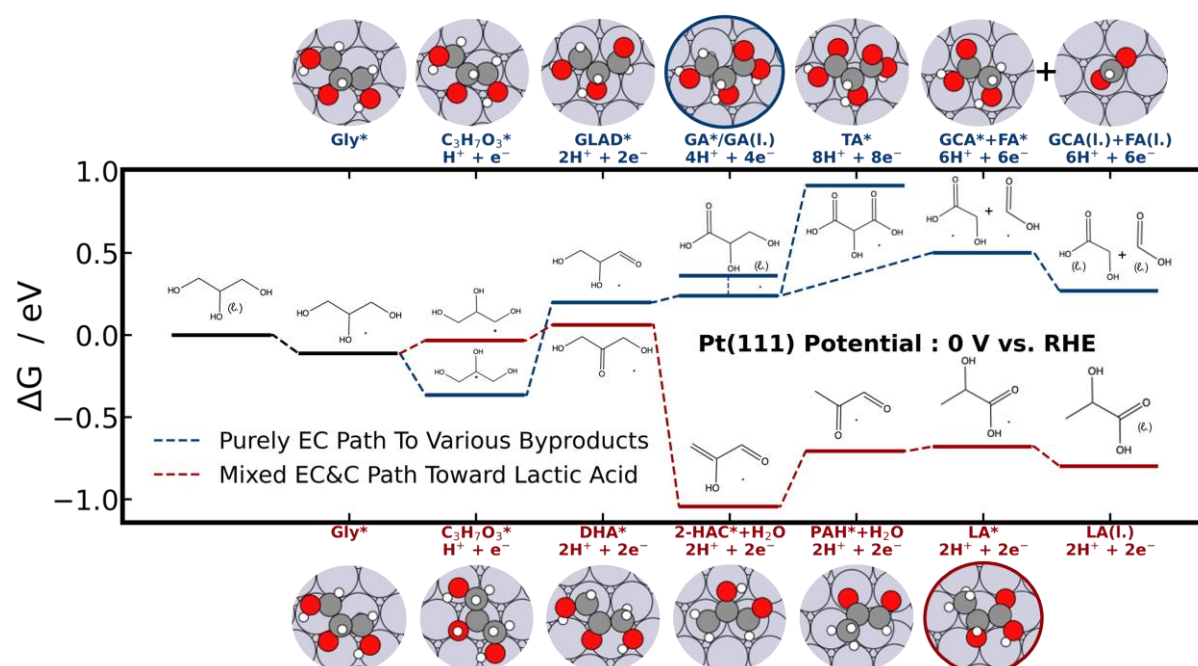


Figure S3. Free energy diagram of glycerol electro-oxidation at Pt(111) at 0 V vs. RHE. Compared to the Fig.4 at 0.5 V vs. RHE

### a) Electrochemical pathway

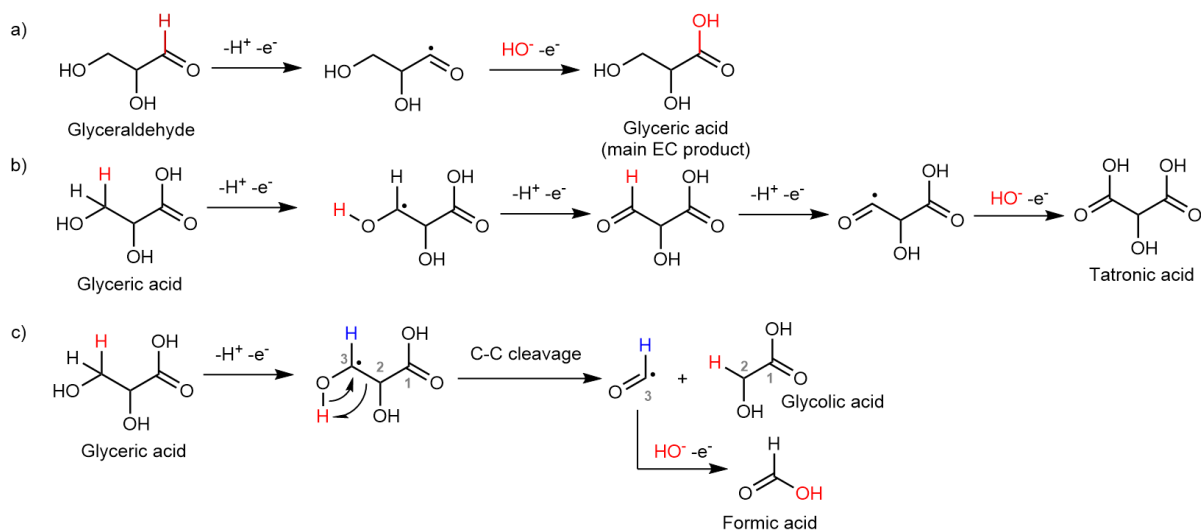


Figure S4: The elementary steps of electrochemical pathway, in a: the mechanism from glyceraldehyde to glyceric acid; in b: the continuous proton-electron transfer mechanism from glyceric acid to tartronic acid; in c: the possible mechanism of C-C splitting, the glyceric acid split into formic acid and glycolic acid.

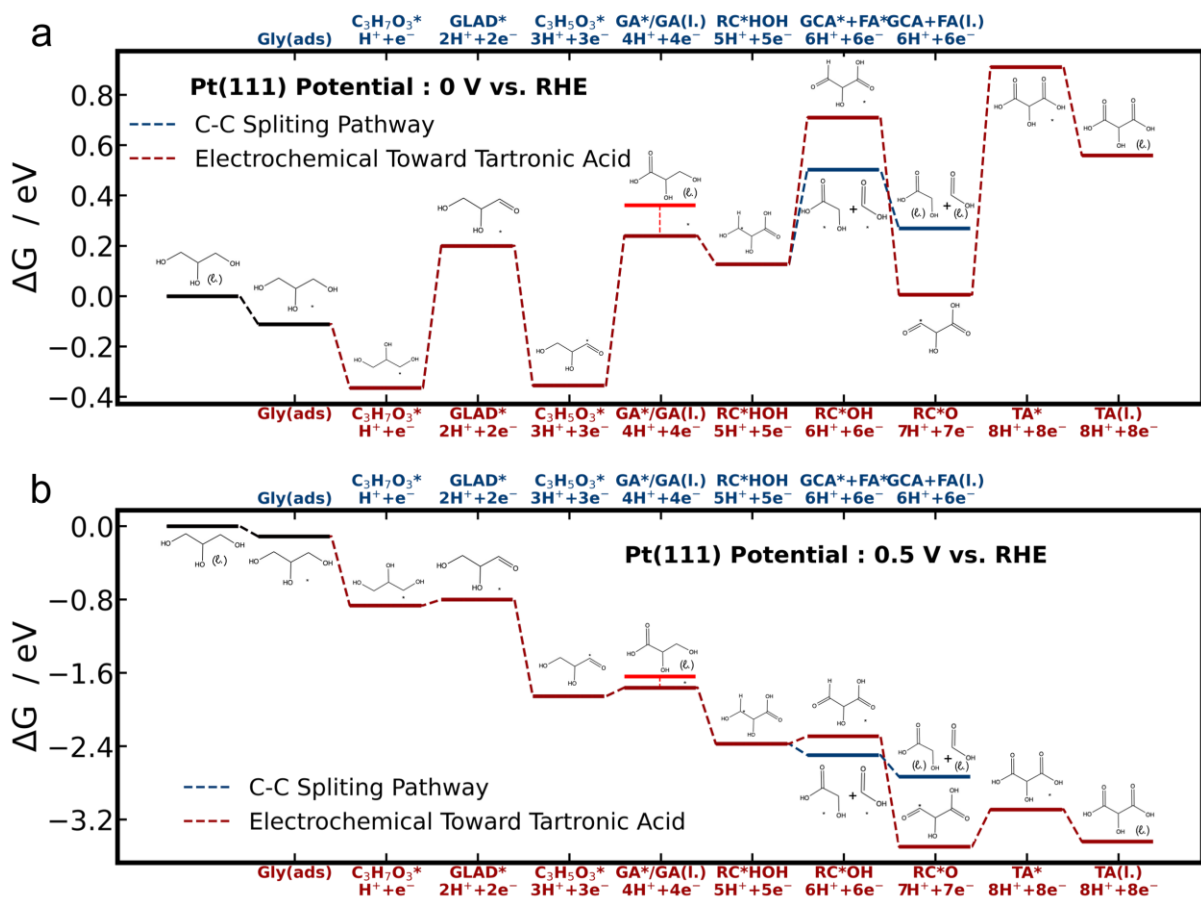


Figure S5 The free energy diagram of elementary electrochemical steps on glycerol electro-oxidation at Pt(111). In different electrode potential condition vs. RHE: a: 0V. b: 0.5V. The bright red bar in the middle is the desorption of glyceric acid. The dark red line is the elementary step toward tartronic acid, the blue line is the steps of C-C splitting.

### 3) Surface Structures and Modelling

In our surface modelling, we built our surface slab based on the XRD and TEM result of the catalyst (In Fig.S2 and Fig.S6). The lattice constant of each metal/metal oxides has been calculated. We built 4 layers  $4 \times 4$  Pt (111) with bottom 2 layers frozen, 4 layers  $4 \times 2$  Anatase- $\text{TiO}_2(101)$  with bottom 2 layers frozen, 3 layers  $\text{CeO}_2(111)$  with bottom 2 layers frozen, and 4 layers  $\gamma\text{-Al}_2\text{O}_3(111)$  with bottom 2 layers frozen. For better accuracy of the surface adsorption calculation, the surface slab located in the centre of cell which the z direction length was  $15 \text{ \AA}$  with the dipole correction. The adsorbate is on the unfixed side of the slab surface, the initial distance between the first layer atom and the adsorbate will set to  $2.5\text{-}3 \text{ \AA}$ . For the KPOINTS,  $4 \times 4 \times 1$ ,  $3 \times 4 \times 1$  and  $3 \times 3 \times 1$   $\gamma$  point centered Monkhorst-Pack k-point grid is applied to sample the Brillouin zone of Pt (111), Anatase- $\text{TiO}_2(101)$ , and  $\text{CeO}_2(111)$ , respectively. For modelling  $\gamma\text{-Al}_2\text{O}_3$ , we used the bulk phase structure from the paper<sup>1</sup> to build  $\gamma\text{-Al}_2\text{O}_3(111)$  surface. Figure S7 shows the clean surface structure we mainly use in this paper. These clean surfaces were applied to calculate the adsorption energy of different adsorbates with sampling at 5 different surface sites.

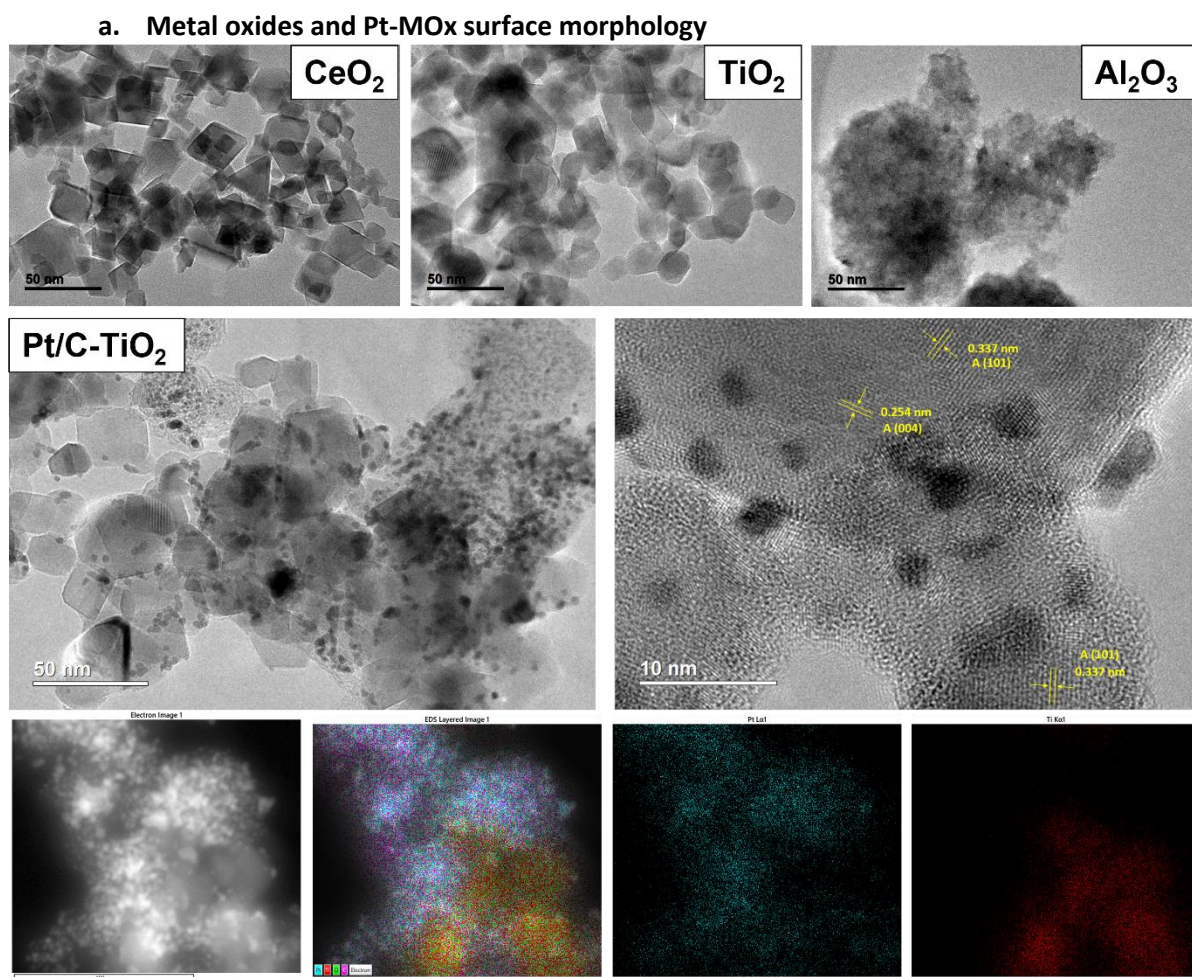


Figure S6. Pt/C-MO<sub>x</sub> multicomponent catalyst morphology.

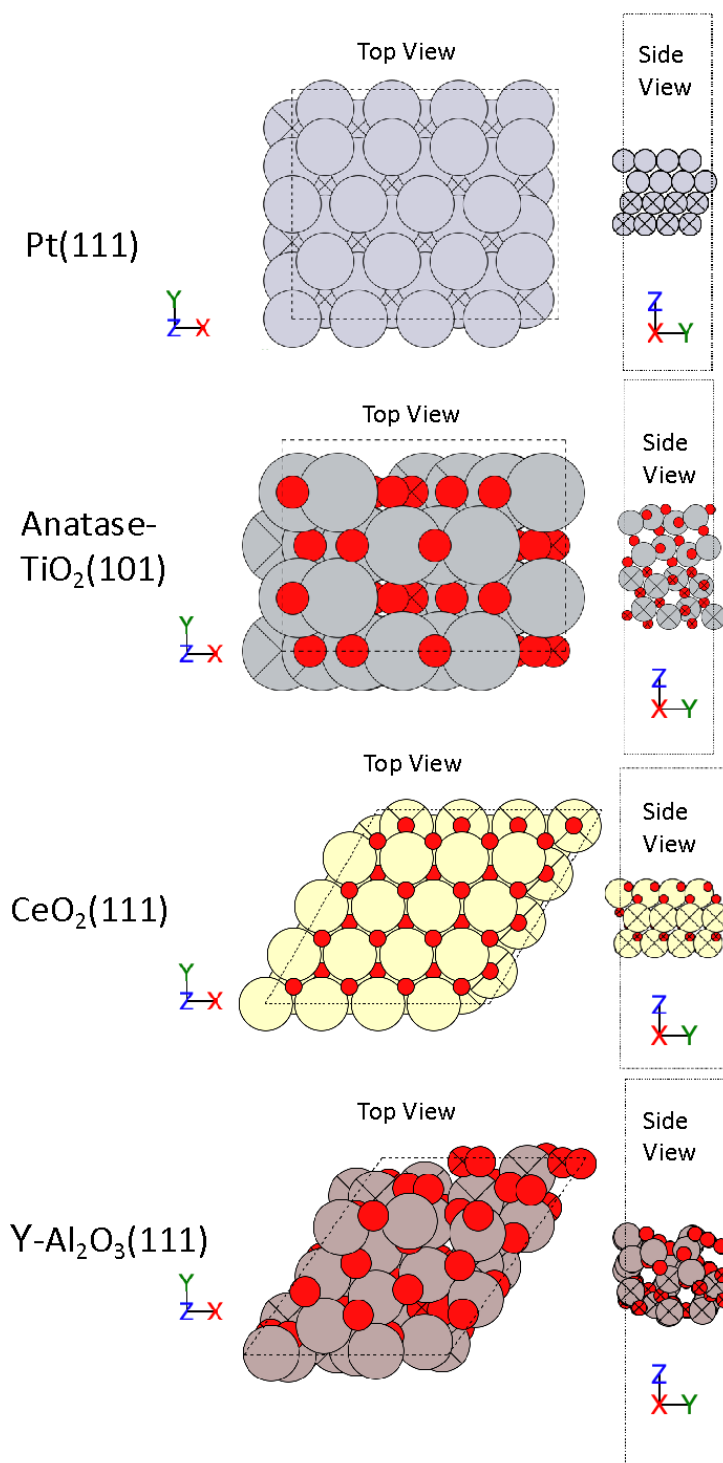


Figure S7 The clean surface structures of Pt(111), Anatase-TiO<sub>2</sub>(101), CeO<sub>2</sub>(111) and  $\gamma$ -Al<sub>2</sub>O<sub>3</sub>(111). These surfaces were applied to calculate the adsorption energy. Color codes for atoms: grey – platinum, silver – titanium, yellow – cerium, pink – aluminium, red – oxygen.

#### 4) Electrolysis Data

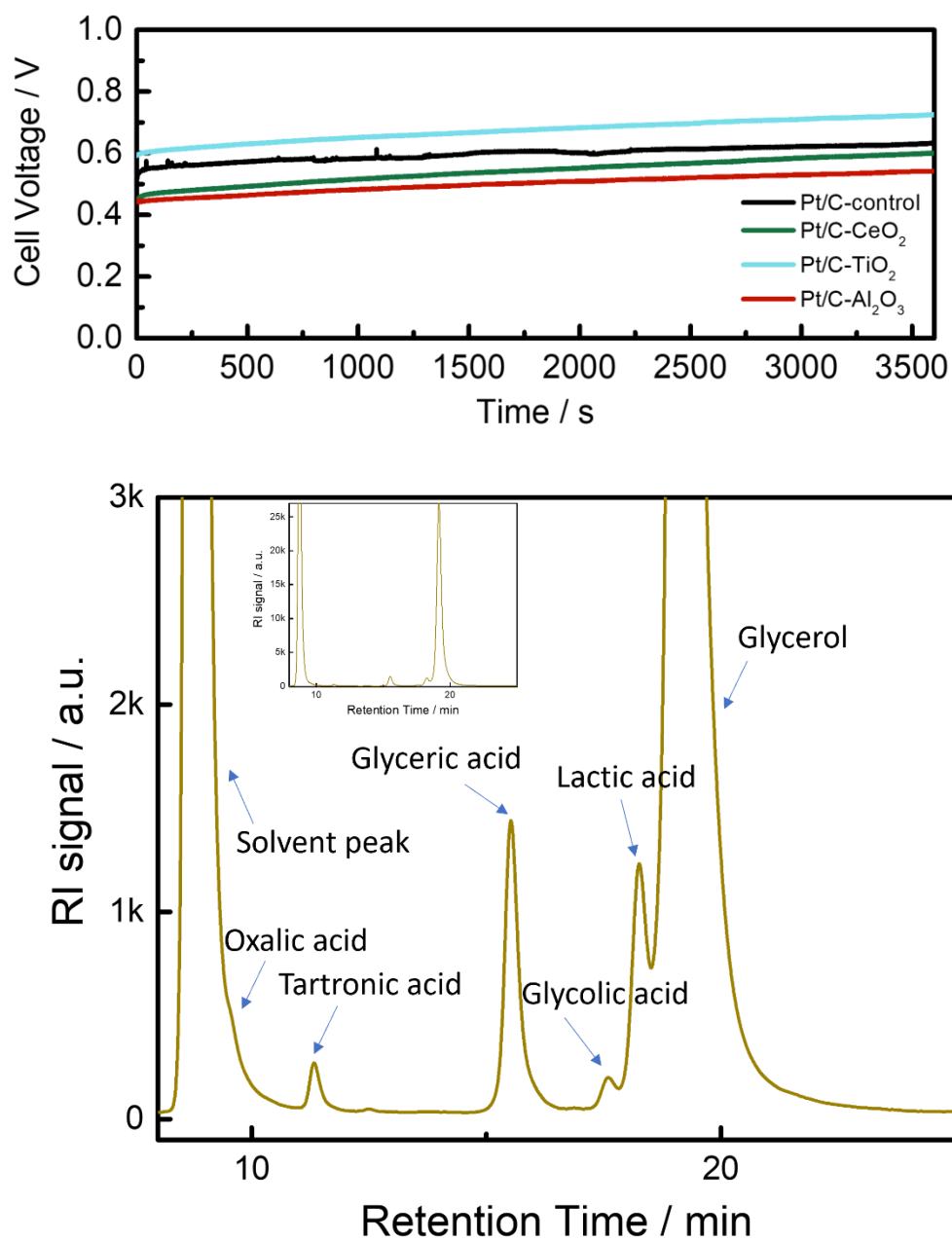


Figure S8. (Top) The corresponding electrolysis data Cell Voltage vs. time on Pt/C and Pt/C with different metal oxides. (Bottom) HPLC chromatograph compound assignment.

## 5) DFT Structures: Relaxed Adsorption Structures

The key to understanding the role of metal oxides from atomic scale is to calculate the adsorption energy of the reaction species. Figure.S9 is relaxed adsorption structures of  $\gamma$ -Al<sub>2</sub>O<sub>3</sub>(111), Anatase-TiO<sub>2</sub>(101) and CeO<sub>2</sub>(111) surface. The surface modelling based on the experimental characterization (Fig. S2 and Fig. S6). At each metal oxides surface and adsorption molecule, we sample 5 different active sites and molecular orientations. The relaxed structures shown in Fig.S9 are the most stable one of each sampling. All the structures and adsorption free energy are in our database, see in Data&Code Availability part.

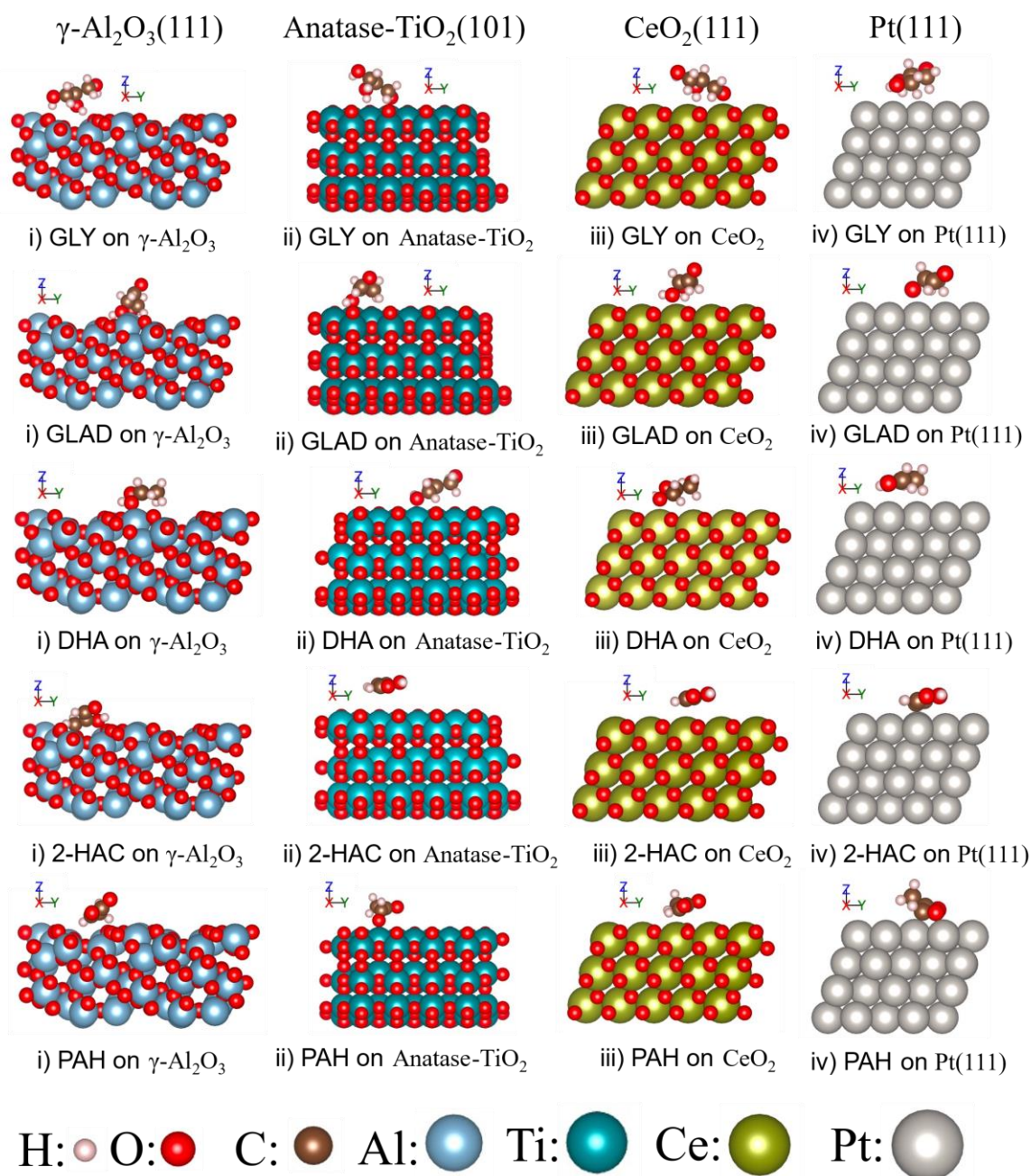


Figure S9. The (Meta-)stable molecules adsorption on different metal oxides, i)  $\gamma$ -Al<sub>2</sub>O<sub>3</sub>(111), ii) Anatase-TiO<sub>2</sub>(101) and iii) CeO<sub>2</sub>(111) surface, shown in each row, respectively. At each column, the structures are for different adsorbates, Glycerol (GLY), Glyceraldehyde (GLAD), Dihydroxyacetone (DHA), 2-hydroxyacrylaldehyde (2-HAC) and Pyruvaldehyde (PAH), respectively. As a comparison, the last column is the adsorbates on Pt(111) surface.

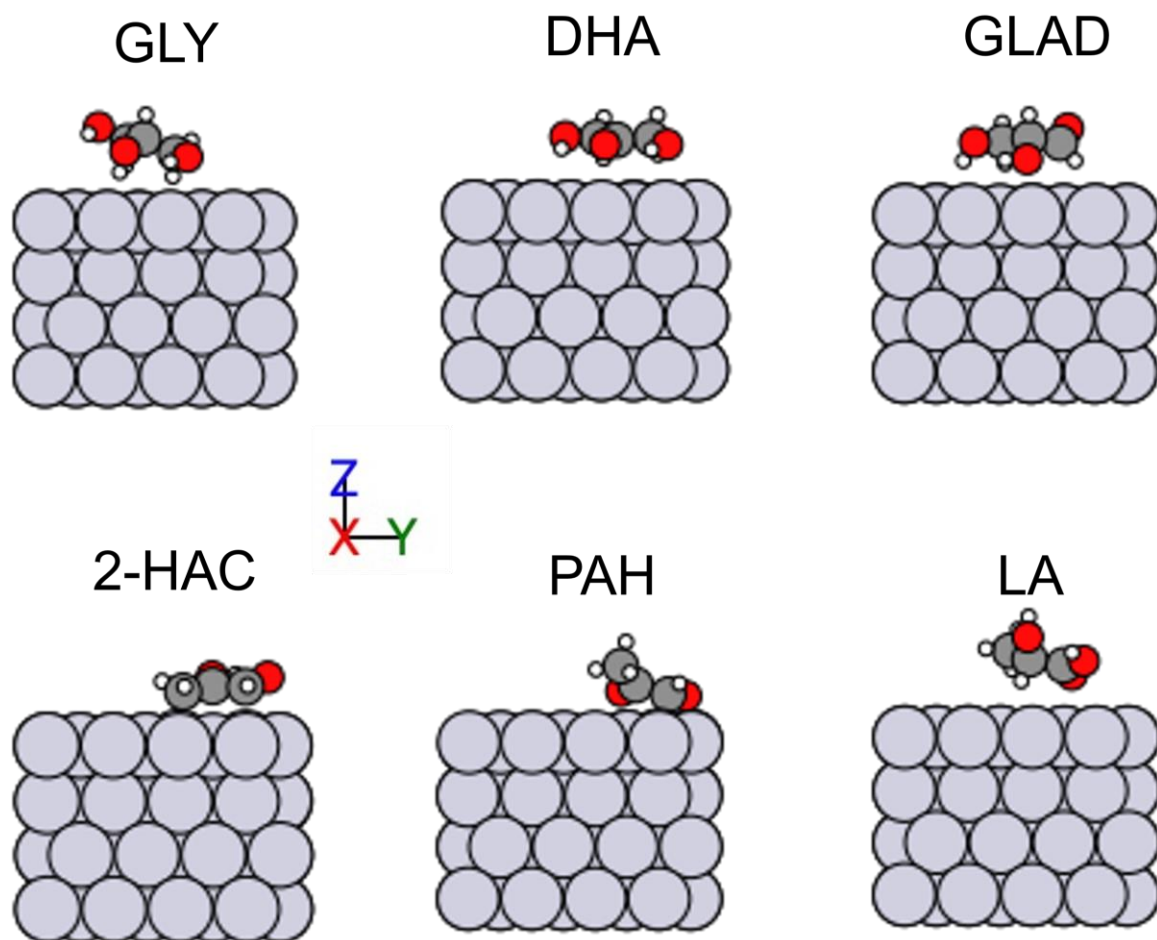


Figure S10. The key intermediate adsorption on Pt(111)

## 6) Surface Acidity and Adsorption Free Energy

### a. BET isotherm

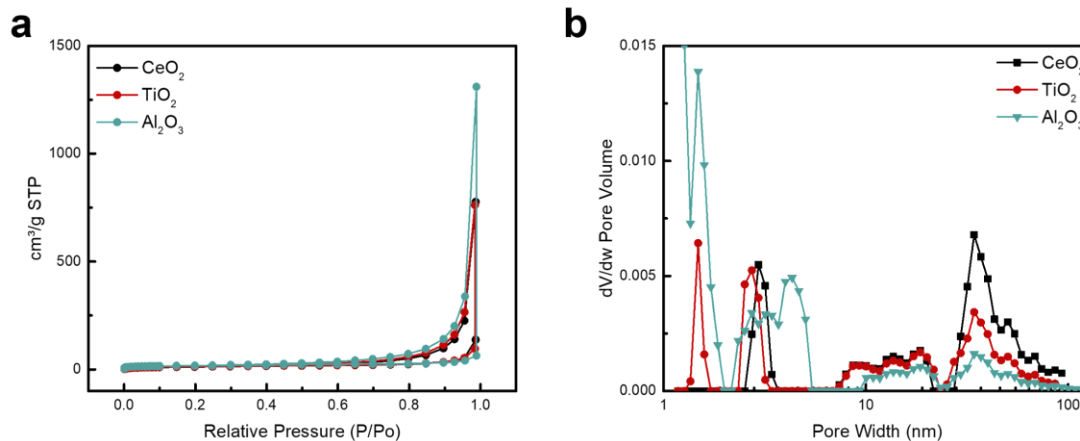


Figure S11. BET isotherm (a) and pore size distribution profile (b) of the MO<sub>x</sub> additives.

Table S1. BET specific area and surface acidic sites of the different additives.

Catalysts additives	BET (m <sup>2</sup> g <sup>-1</sup> )	Surface acidic sites (mmol g <sup>-1</sup> )
Carbon black	62	0.012
CeO <sub>2</sub>	45	0.195
TiO <sub>2</sub>	51	0.252
Al <sub>2</sub> O <sub>3</sub>	63	0.490

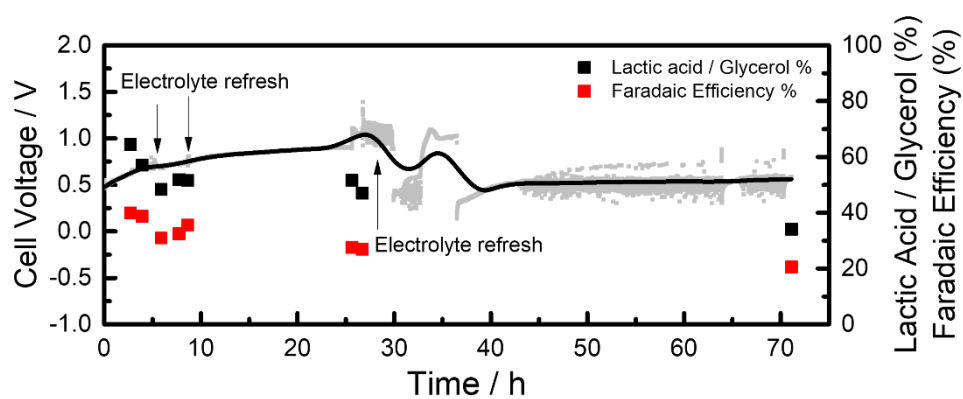


Fig S12. Extended stability measurement of the glycerol electrolysis process. Current density: 20 mA cm<sup>-2</sup>. Temperature: 60 °C. Anolyte: 1 M Glycerol/1 M NaOH; catholyte: 1 M NaOH.

### b. NH<sub>3</sub>-TPD results

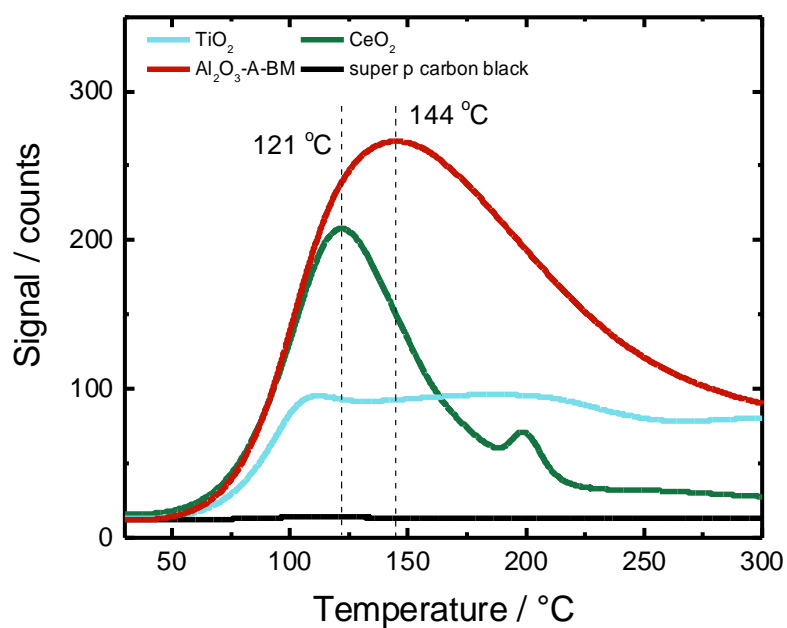


Figure S13. Experimental  $\text{NH}_3$ -TPD profile on different surfaces: carbon black,  $\text{TiO}_2$ ,  $\text{CeO}_2$  and  $\text{Al}_2\text{O}_3$ .

c.  $\text{NH}_3$ -DHA/GLAD adsorption free energy

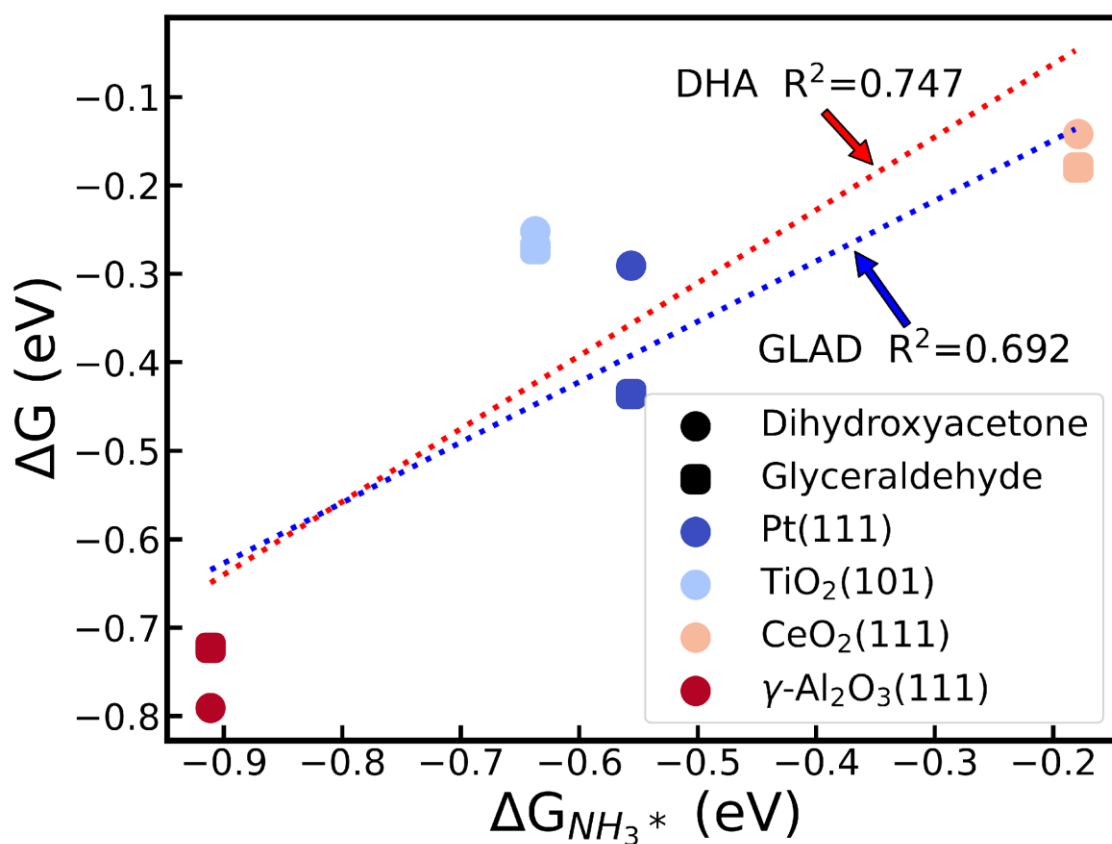


Figure S14. The adsorption free energy of DHA(Circle) and GLAD (Square) vs. the ammonia adsorption free energy.

## 7) Computational details

### a. DFT Parameters and Description

In this paper, we use Vienna Ab initio simulation package (VASP)<sup>2</sup> for the atomic scale modelling from first principle. The projector-augmented-wave (PAW)<sup>3</sup> formalism was introduced to re-expand the electron density in the reciprocal space. The energy cutoff of valence electrons were set up to 500eV and the Methfessel-Paxton smearing with width of 0.2 eV was used. We employed revised Perdew–Burke–Ernzerhof (RPBE)<sup>4</sup> functional to describe the exchange-correlation effects, which works well in surface. For the long-term interaction / dispersion correction, the Grimme D3<sup>5</sup> was applied in all the calculations, because the van der Waals attraction between biomass carbon chain and the surface should be well considered and described.<sup>6</sup>

The kpoint sampling<sup>7</sup> 3x3x1 used for metal oxides CeO<sub>2</sub>(111) and  $\gamma$ -Al<sub>2</sub>O<sub>3</sub>(111), and 3x4x1 used for Pt(111) and Anatase-TiO<sub>2</sub>(101) surfaces. The surface structures are shown in Fig. S7

To evaluate the active sites and different molecule orientation at surface, all the surface adsorption structures were sampled in 5 different initial position/sites on metal / metal oxides surfaces. In some cases, due to the bad initial guess of the structures, the C3 chain will split under DFT relaxation which is not reasonable in real catalysis (C-C splitting is not the main reaction). We ignored the C-C splitting structures when calculating the adsorption energy. The adsorption energy was calculated by the average of all the stable structures we sampled. The data showed in our [github](#). Link in SI part 1.

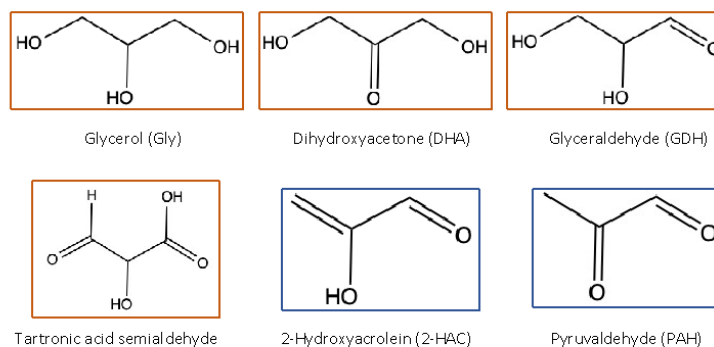
Considering the metal oxides calculations, we compared the DFT and DFT+ U on Anatase-TiO<sub>2</sub>(101) surface. We benchmarked the U values on bulk Anatase-TiO<sub>2</sub>. On the glycerol species adsorption, we found that with or without U correction the results are almost the same. Thus in our calculation, we used DFT (not +U) to calculate all the adsorption energy on metal oxides surface.

For the free energy calculation, the zero-point energy, entropy correction was from the ab-initio frequency from VASP (IBRION=5), which is the second order derivatives of the energy with different position of the ions using finite differences approach. The cutoff frequency is 12 cm<sup>-1</sup>. For the surface adsorbates, we used Harmonic limit approximation to calculate the energy. For the molecules in gas phase, we used ideal gas approximation to calculate the energy.<sup>8</sup> The temperature used in free energy calculation was set as experimental temperature (60°C, ~333K). The computational hydrogen electrode (CHE)<sup>9</sup> model was applied to calculate the electron transfer steps in the free energy diagram.

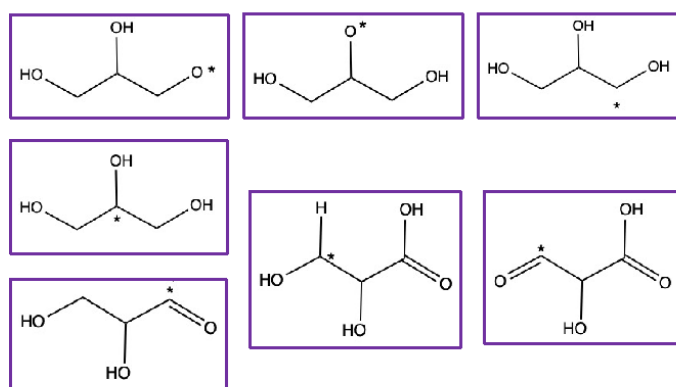
### b. Adsorbates, Key Intermediates, Reference States

In our DFT calculation, we calculated the (meta)stable molecules, key intermediates, and the intermediates of Proton-Couple Electron Transfer (PCET) in the first 2 steps at Pt (111). For the high band gap of metal oxides, the electron transfer step prefers to occur at the Pt surface, so that we calculate the key intermediates inside the selectivity steps toward lactic acid. The reference states in our calculation are glycerol molecule (C<sub>3</sub>H<sub>8</sub>O<sub>3</sub>), hydrogen gas (H<sub>2</sub>), and water molecule (H<sub>2</sub>O). All the reference states are in gas phase. For glycerol and water, we used the pressure of saturated vapor pressure in experimental temperature (ca. 333K). For hydrogen gas, we used 1 atm as reference pressure. For the electrochemical system, we used computational hydrogen electrode (CHE) as reference.<sup>9</sup> Figure S6 shows the molecules and intermediates we considered and calculated in this paper.

(Meta-)Stable Species:



Intermediates:



Products:

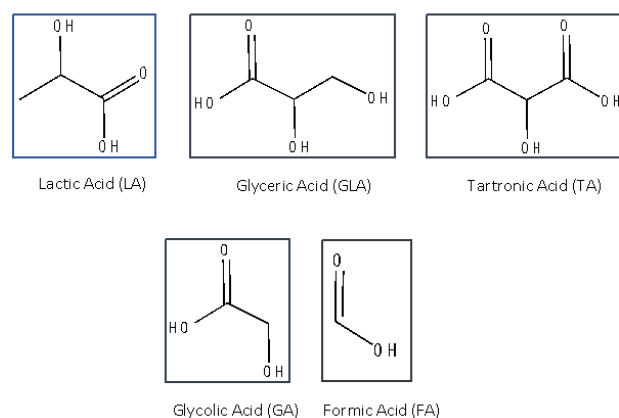


Figure S15 The adsorbates list in DFT calculation. In the first block, they are (Meta-)Stable species which are the closed shell organic compounds that exist on surface (in orange rectangle) and the precursor of Lactic acid (in blue rectangle). The second block is all the possible intermediates (in purple rectangle) of the proton-couple electron transfer step, with the symbol \* marking the atom bound the surface. In the third block, they are products of glycerol oxidation which are electrochemical-chemical products (in blue rectangle) and fully electro-oxidation products (in gray rectangle).

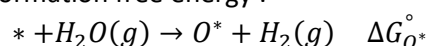
c. Pourbaix Diagram of Metal Oxides & Surface Acidity

Under electrochemical condition, the electrode potential will affect the surface phase component, especially for metal oxides. In aqueous solution, the surface will cover with some  $O^*$  or  $OH^*$  species when increasing the electrode potential (Surface Oxides formation). The two extreme cases are metal-terminated and oxygen-terminated surface.

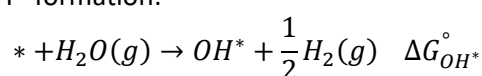
We calculated the Pourbaix Diagram of metal oxides by DFT and used metal-terminated surface as initial structure. For Anatase-TiO<sub>2</sub>(101), we use 4x2x4(bottom 2 layers are frozen) unit cell to calculate the Pourbaix Diagram and the kpoints is 3x6x1. For CeO<sub>2</sub>(111), we use 2x2x3(bottom 2 layers are frozen) to calculate the Pourbaix Diagram and the kpoints is 5x5x1.

For  $\gamma$ -Al<sub>2</sub>O<sub>3</sub>(111), we use the structure shown in Figure S7 to calculate the Pourbaix Diagram. For the accurate results and considering the adsorbates-adsorbates interaction, we sample the traversal combinations of the surface active sites. The surface active site here is the unsaturated metal surface atoms, which means the coordination number is less than 6(4 in some cases). We marked different unsaturated metal top sites as A,B,C,... and put the O\* or OH\* on the top sites with the distance between 2-3 Å as initial structure. The reference state is H<sub>2</sub>O and H<sub>2</sub> in gas phase.

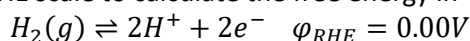
For the surface O\* formation free energy :



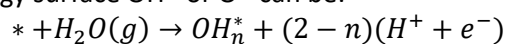
For the surface OH\* formation:



Considering the effect of electrode potential and pH effect in solution phase, we apply CHE<sup>9</sup> model and RHE scale to calculate the free energy in



So, the free energy surface OH\* or O\* can be:



$$\Delta G_{OH_n^*}(U_{RHE}) = \Delta G_{OH_n^*}^\circ + (2 - n)eU_{RHE}$$

Where n=0 or n=1, representing O\* and OH\*, respectively.

From the Pourbaix diagram in Fig. S15, under the experimental condition (ca. 0.4V-0.8V vs. RHE), there is no extra O\* and OH\* adsorption at Anatase-TiO<sub>2</sub>(101) and CeO<sub>2</sub>(111) surface. However, at  $\gamma$ -Al<sub>2</sub>O<sub>3</sub>(111) surface, there is small coverage of OH\* on the surface with weak adsorption under experimental potential condition.

To convert the Pourbaix diagram into coverage dependence, we select the lowest free energy one at each coverage we sampled:

$$\Delta G_{OH_n^*,min}^\circ(\theta) = \min \{ \cup \Delta G_{OH_n^*}^\circ(\theta) \}$$

The Pourbaix diagram under different coverage and potential will be plotted by:

$$\Delta G_{OH_n^*,min}(U_{RHE}, \theta) = \Delta G_{OH_n^*,min}^\circ(\theta) + (2 - n)eU_{RHE}$$

We tested the surface acidity from DFT calculation by the adsorption/desorption energy of ammonia, which could compare with ammonia TPD from experimental results. We sampled different surface sites of NH<sub>3</sub> adsorption and compared the acidity different among the surface sites.

For the Anatase-TiO<sub>2</sub>(101), we sampled 2 different top sites of Ti atom to test the acidity. For the CeO<sub>2</sub>(111) and Pt (111), we sampled 1 top site of metal atoms because the metal is FCC packed. For  $\gamma$ -Al<sub>2</sub>O<sub>3</sub>, we sampled 5 sites for testing the surface acidic. The surface acidic site here is the unsaturated metal surface atoms, which means the coordination number is less than 6(4 in some cases) and just mentioned in SI part 2.d, the same sites we sampled in Pourbaix diagram. These sites will consider as intrinsic acidic sites.

For rational construing the metal oxides surface, first, we constructed rational MO<sub>x</sub> structure models based on the morphological and physical characterisation presented in Fig 5 and S2, S6. The most stable surface structures were then chosen to study the Pourbaix diagrams at reaction conditions, which we show in Fig SI. From our results, the most stable surfaces at our experimental conditions (0.5-0.6V vs. RHE) are anatase - TiO<sub>2</sub>(101) with the O\* species occupying the Ti-bridge sites and CeO<sub>2</sub>(111) with O\* in the

fcc hollow sites. The  $\gamma\text{-Al}_2\text{O}_3$  unit cell obtained from literature, where we determine the most stable surface at reaction conditions is  $\gamma\text{-Al}_2\text{O}_3(111)$  with 0.4 ML of  $\text{OH}^*$  ( $\gamma\text{-Al}_2\text{O}_3(111)\text{-OH}$ ). The  $\text{OH}^*$  coverage strongly influences the binding properties of the surface, as  $\text{OH}^*$  tends to block the acidic sites that are, responsible for  $\gamma\text{-Al}_2\text{O}_3$  catalytic ability, as we will discuss in detail below. We note that the highest surface acidity of  $\gamma\text{-Al}_2\text{O}_3(111)$  leads to a tendency of its sites to be covered by  $\text{OH}^*$  at reaction conditions (0.4-0.7 V vs. RHE). However, as we show in Fig. S16, key intermediates toward lactic acid adsorb even stronger on the surface, replacing  $\text{OH}^*$  at moderate reaction conditions. Thus, the surface model of  $\gamma\text{-Al}_2\text{O}_3(111)$  is more representative than  $\gamma\text{-Al}_2\text{O}_3(111)\text{-OH}$ .

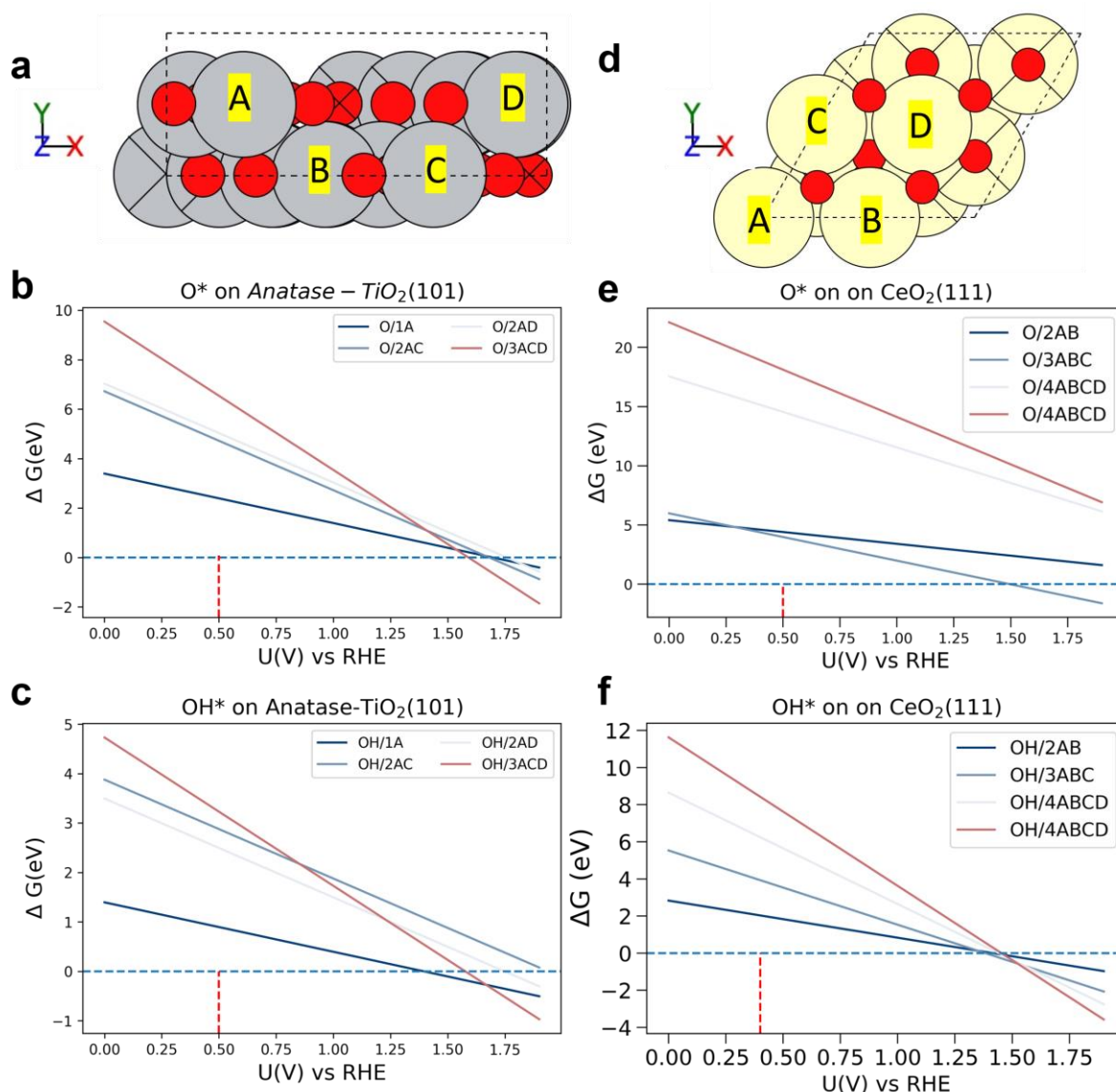


Figure S16 The Pourbaix diagram of Anatase- $\text{TiO}_2(101)$  and  $\text{CeO}_2(111)$ . The clean surface structures that applied to calculate the Pourbaix diagram showed in a: Anatase- $\text{TiO}_2(101)$  and in d:  $\text{CeO}_2(111)$ . The top sites were marked as the capital letter. In b and c: the Pourbaix diagram of  $\text{O}^*$  and  $\text{OH}^*$  adsorption at Anatase- $\text{TiO}_2(101)$ . In e and f: the Pourbaix diagram of  $\text{O}^*$  and  $\text{OH}^*$  adsorption at  $\text{CeO}_2(111)$ . The labels inside panels b,c,e,f are the sampling of active sites corresponding to the capital letter marked in a,d.

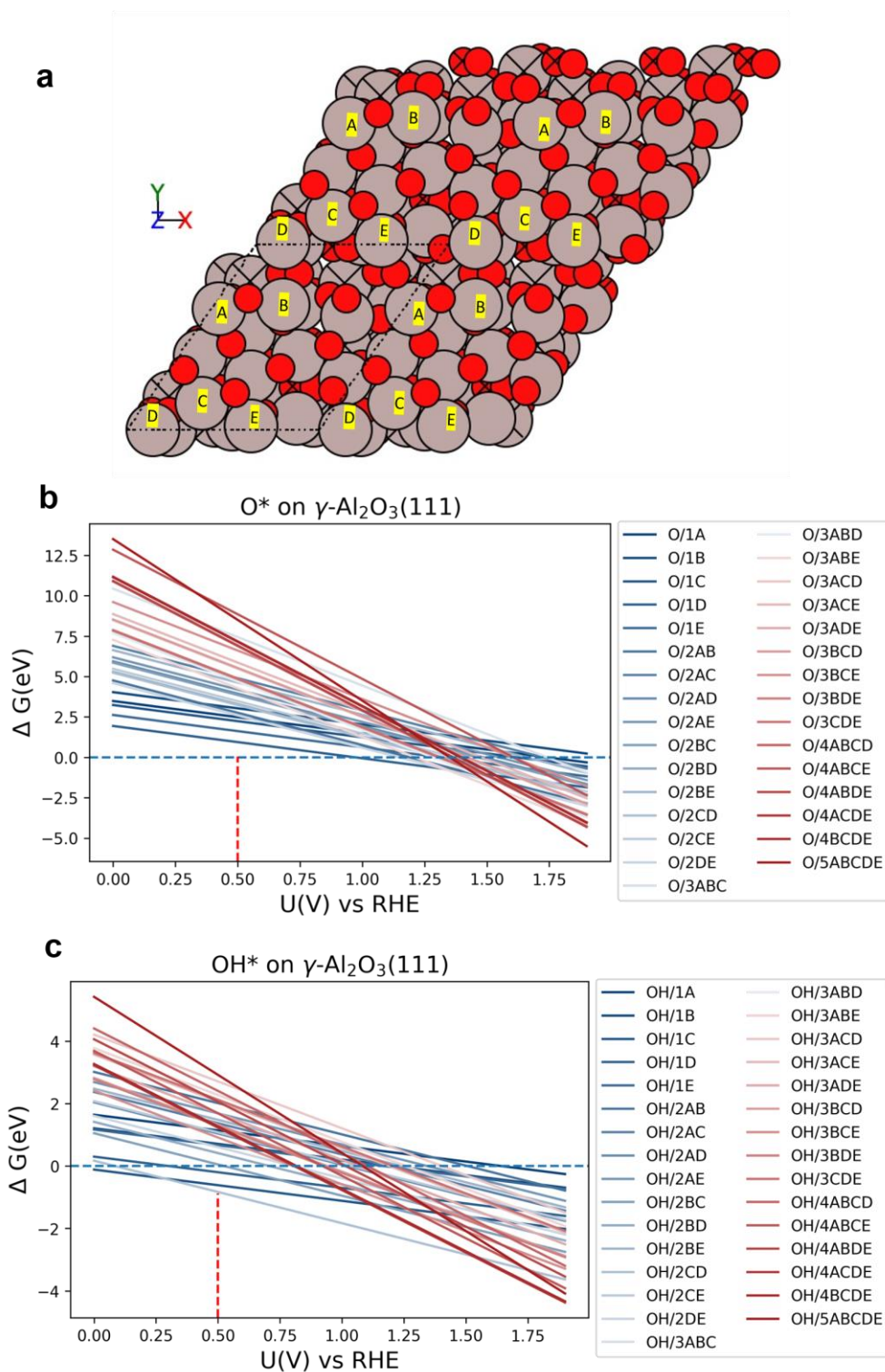


Figure S17 The Pourbaix diagram of  $\gamma\text{-Al}_2\text{O}_3(111)$ , The clean surface structures that applied to calculate the Pourbaix diagram showed in a. The unsaturated sites were marked as the capital letter. In b: the Pourbaix diagram of O\* adsorption at  $\gamma\text{-Al}_2\text{O}_3(111)$  with each line that sampling from different acidic sites. In c: the Pourbaix diagram of OH\* adsorption at  $\gamma\text{-Al}_2\text{O}_3(111)$ . The labels of the panels b,c are the sampling of active sites corresponding to the capital letter marked in a.

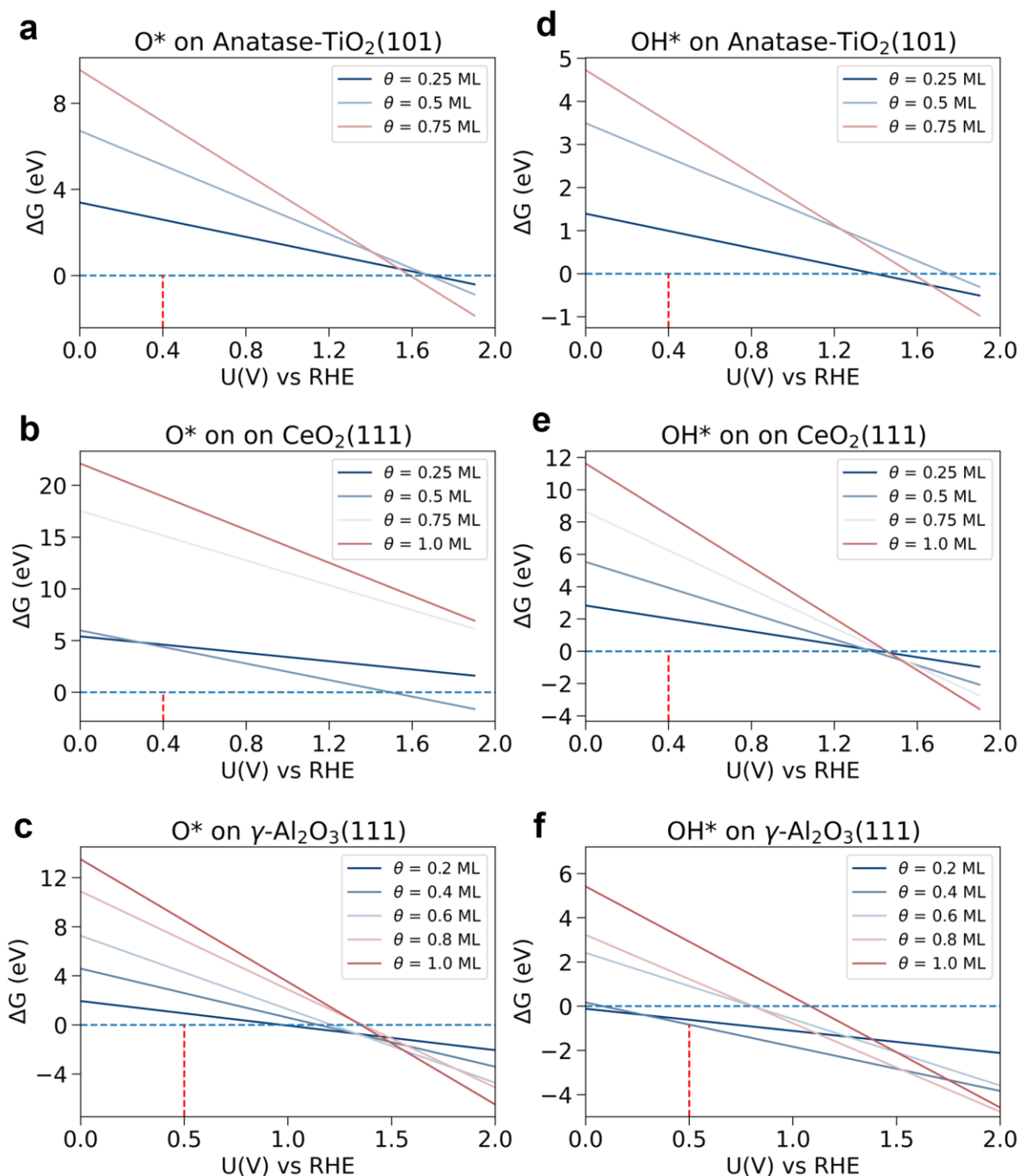


Figure S18 The Pourbaix diagram via coverage of Anatase-TiO<sub>2</sub>(101), CeO<sub>2</sub>(111) and  $\gamma$ -Al<sub>2</sub>O<sub>3</sub>(111). In a,b,c: the O\* adsorption free energy vs. electrode potential. In d,e,f: the OH\* adsorption free energy vs. electrode potential

#### d. Adsorption Energy, formation energy and Free Energy

Regarding the potential energy by the references of Glycerol(C<sub>3</sub>H<sub>8</sub>O<sub>3</sub>), H<sub>2</sub>O and H<sub>2</sub>. All the reference states are in gas phase. For different species, the formation energy is:

$$E(C_nH_mO_l) = nE(C) + mE(H) + lE(O)$$

Where  $E(C_nH_mO_l)$  is the formation energy of species  $C_nH_mO_l$  and n,m,l are stoichiometric number of C,H,O atoms.  $E(C)$ ,  $E(H)$  and  $E(O)$  are the potential energy of reference atom which are calculated from DFT and reference molecules. Each of the

reference molecule was set in the center of a vacuum box whose volume is  $15 \times 15 \times 15 \text{ \AA}^3$  and the KPOINTS was  $1 \times 1 \times 1$ .

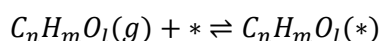
The reference energy of atoms is:

$$E(C) = \frac{1}{3}E(C_3H_8O_3) - E(H_2O) - \frac{3}{2}E(H_2)$$

$$E(O) = E(H_2O) - E(H_2)$$

$$E(H) = \frac{1}{2}E(H_2)$$

For every adsorbate we mentioned in b, the chemical equation of the adsorption process is:



Where \* represents the surface site(s).

We calculated the adsorption energy of a species by:

$$\Delta E_{ads}(C_nH_mO_l) = E_{slab+ads} - E_{slab} - E(C_nH_mO_l)$$

Where  $E_{slab+ads}$  is the potential energy of the system (surface + adsorbate),  $E_{slab}$  is the potential energy of clean surface,  $E(C_nH_mO_l)$  is the formation energy of adsorbate we just mentioned above.

The free energy was calculated by ASE thermochemistry<sup>10</sup>. For reference molecules and stable species, we use Idea-gas limit. For the adsorbates, we use Harmonic limit. The vibration frequency was calculated by VASP (IBRION=5) which as an input to ASE thermochemistry. For the adsorbate frequency, we just calculated the frequency of adsorbate atoms and fixed the surface because the contribution of phonon inside metal/metal oxides are neglectable compared to the vibration of adsorbates. The free energy of slab+ads is:

$$G_{slab+ads} = E_{slab+ads} + ZPE + C_v - TS$$

Where ZPE is the zero-point energy,  $C_v$  is the constant volume heat capacity,  $T$  is the absolute temperature in K,  $S$  is the entropy. From the experimental condition, the temperature maintained in  $60^\circ\text{C}$ . So we set the temperature as  $333\text{K}$  for every calculation. Considering the free energy of the stable molecules, we use the formation free energy of each molecule to calculate the energy in free energy diagram. In experimental condition, the reaction occurs in solution phase. To match the solution condition, we use vapor pressure of the Glycerol and  $\text{H}_2\text{O}$  to calculate the reference free energy. Hydrogen gas is always in gas phase, so we set the pressure as  $1 \text{ atm}$ . The reference free energy was calculated by the DFT results and thermodynamic data (tabulated in part g):

$$G_{molecule}(T, P) = E_{molecule} + ZPE + C_v - TS + k_B T \ln\left(\frac{P_{vap,molecule}}{P^\circ}\right)$$

Where  $P^\circ$  is the standard pressure( $1 \text{ atm}$ ),  $k_B$  is the Boltzmann constant.

The formation free energy of the intermediates was calculated by the reference states:

$$G(C_nH_mO_l) = nG(C) + mG(H) + lG(O)$$

The free energy of each atom is:

$$G(C) = \frac{1}{3}G(C_3H_8O_3) - G(H_2O) - \frac{3}{2}G(H_2)$$

$$G(O) = G(H_2O) - G(H_2)$$

$$G(H) = \frac{1}{2}G(H_2)$$

In the free energy diagram (FED), the reference states are each surface and the reference molecules we mentioned above. The Gas phase Glycerol, H<sub>2</sub>, H<sub>2</sub>O and clean surface is the starting point of FED which is 0. The endpoint of FED is the gas phase products. The overall Gibbs free energy of the reaction are calculated by DFT of the gas phase molecule:

$$\Delta G_{reaction} = G_{products} - G_{reactant}$$

In FED, the free energy and Pourbaix diagram plot in each reaction step is:

$$G_{Step} = G_{Slab+ads} - E_{Slab} - G(C_nH_mO_l)$$

In the Pt and metal oxides, considering the key intermediates that will competitively desorb and re-adsorb among catalysis surfaces. We use the adsorption free energy, which reference to each adsorbates' molecules.

The adsorption energy is:

$$\Delta E_{ads,mole}(C_nH_mO_l(g)) = E_{slab+ads} - E_{slab} - E_{mole}(C_nH_mO_l(g))$$

Where  $E_{mole}(C_nH_mO_l(g))$  is the potential energy of molecule in gas phase. In DFT calculation, each of the molecule was set in the center of a vacuum box whose volume is 15x15x15Å<sup>3</sup> and the KPOINTS was 1x1x1. Considering the experimental condition, we use vapor pressure to calculate the free energy of molecules in solution(liquid) phase, as an approximation. In the plot of molecule adsorption (Fig. 4), the adsorption free energy is:

$$\Delta G_{ads,mole}(C_nH_mO_l(l.)) = G_{Slab+ads} - E_{Slab} - G(C_nH_mO_l(l.))$$

#### e. Tabulated the Thermodynamic Data

The vapor pressure of the molecules we used in this paper to calculate the free energy.

Molecule	Equilibrium Vapor Pressure	Source
Glycerol	25 Pa	11
Glycolic Acid	1080 Pa(80 °C)	12
Glyceric Acid	293 Pa (25 °C)	ChemSrc
Formic Acid	5333 Pa	13
Tartronic Acid	0.00025 Pa	14
Lactic Acid	ca. 10 Pa	lambic.info
H <sub>2</sub> O	3282 Pa	13
H <sub>2</sub> (g)	101325Pa	1 atm
NH <sub>3</sub> (g)	101325Pa	1 atm

The point group and symmetry number of molecules that is applied to calculate the thermal properties of adsorption structures<sup>15</sup>

Molecules	Point group	Symetry Number
NH <sub>3</sub>	C <sub>3v</sub>	3
Glycerol	C <sub>s</sub>	1
Dihydroxyacetone	C <sub>2h</sub>	2
Glyceraldehyde	C <sub>1</sub>	1
2-Hydroxyacrolein	C <sub>s</sub>	1
Pyruvaldehyde	C <sub>s</sub>	1
Lactic Acid	C <sub>1</sub>	1

Glyceric Acid	C <sub>1</sub>	1
Tartronic Acid	C <sub>s</sub>	1
Glycolic Acid	C <sub>s</sub>	1
Formic Acid	C <sub>s</sub>	1
H <sub>2</sub> O	C <sub>2v</sub>	2
H <sub>2</sub>	D <sup>∞</sup> <sub>h</sub>	2

- 1 Gu, J., Wang, J. & Leszczynski, J. Structure and Energetics of (111) Surface of  $\gamma$ -Al<sub>2</sub>O<sub>3</sub>: Insights from DFT Including Periodic Boundary Approach. *ACS Omega* **3**, 1881-1888 (2018). <https://doi.org/10.1021/acsomega.7b01921>
- 2 Kresse, G. & Furthmüller, J. Efficient iterative schemes for ab initio total-energy calculations using a plane-wave basis set. *Physical Review B* **54**, 11169-11186 (1996). <https://doi.org/10.1103/PhysRevB.54.11169>
- 3 Kresse, G. & Joubert, D. From ultrasoft pseudopotentials to the projector augmented-wave method. *Physical Review B* **59**, 1758-1775 (1999). <https://doi.org/10.1103/PhysRevB.59.1758>
- 4 Hammer, B., Hansen, L. B. & Nørskov, J. K. Improved adsorption energetics within density-functional theory using revised Perdew-Burke-Ernzerhof functionals. *Physical Review B* **59**, 7413-7421 (1999). <https://doi.org/10.1103/PhysRevB.59.7413>
- 5 Grimme, S., Antony, J., Ehrlich, S. & Krieg, H. A consistent and accurate ab initio parametrization of density functional dispersion correction (DFT-D) for the 94 elements H-Pu. *The Journal of Chemical Physics* **132**, 154104 (2010). <https://doi.org/10.1063/1.3382344>
- 6 Tait, S. L., Dohnálek, Z., Campbell, C. T. & Kay, B. D. n-alkanes on MgO(100). I. Coverage-dependent desorption kinetics of n-butane. *The Journal of Chemical Physics* **122**, 164707 (2005). <https://doi.org/10.1063/1.1883629>
- 7 Monkhorst, H. J. & Pack, J. D. Special points for Brillouin-zone integrations. *Physical Review B* **13**, 5188-5192 (1976). <https://doi.org/10.1103/PhysRevB.13.5188>
- 8 Cramer, C. J. & Bickelhaupt, F. Essentials of computational chemistry. *ANGEWANDTE CHEMIE-INTERNATIONAL EDITION IN ENGLISH-* **42**, 381-381 (2003).
- 9 Nørskov, J. K. *et al.* Origin of the Overpotential for Oxygen Reduction at a Fuel-Cell Cathode. *The Journal of Physical Chemistry B* **108**, 17886-17892 (2004). <https://doi.org/10.1021/jp047349j>
- 10 Hjorth Larsen, A. *et al.* The atomic simulation environment—a Python library for working with atoms. *Journal of Physics: Condensed Matter* **29**, 273002 (2017). <https://doi.org/10.1088/1361-648x/aa680e>
- 11 Cammenga, H. K., Schulze, F. W. & Theuerl, W. Vapor pressure and evaporation coefficient of glycerol. *Journal of Chemical and Engineering Data* **22**, 131-134 (1977).
- 12 Daubert T, E. Physical and Thermodynamic Properties of Pure Chemicals : Data Compilation. *Design Institute for Physacal Property Data(DIPPR)* (1989).
- 13 Haynes, W. M., Lide, D. R. & Bruno, T. J. *CRC handbook of chemistry and physics*. (CRC press, 2016).
- 14 Booth, A. M. *et al.* Solid state and sub-cooled liquid vapour pressures of substituted dicarboxylic acids using Knudsen Effusion Mass Spectrometry (KEMS) and Differential Scanning Calorimetry. *Atmos. Chem. Phys.* **10**, 4879-4892 (2010). <https://doi.org/10.5194/acp-10-4879-2010>
- 15 Cramer, C. J. *Essentials of computational chemistry: theories and models*. (John Wiley & Sons, 2013).

